IEEE Access
Multidisciplinary ⋮ Rapid Review ⋮ Open Access Journal

Received 24 February 2023, accepted 13 March 2023, date of publication 16 March 2023, date of current version 22 March 2023.

Digital Object Identifier 10.1109/ACCESS.2023.3257847

RESEARCH ARTICLE

Energy and Spectral Efficiencies of Cell-Free Millimeter-Wave Massive MIMO Systems Under Rain Attenuation Based on Ray Tracing Simulations

HIGO THAIAN P. DA SILVA[1], HUGERLES S. SILVA[2,3], (Member, IEEE), MARCELO S. ALENCAR[4,5], (Senior Member, IEEE), WAMBERTO J. L. DE QUEIROZ[1], AND UGO SILVA DIAS[3], (Senior Member, IEEE)

[1]Department of Electrical Engineering, Federal University of Campina Grande (UFCG), Campina Grande 58429-900, Brazil
[2]Institute of Telecommunications and Department of Electronics, Telecommunications and Informatics, University of Aveiro, Campus Universitário de Santiago, 3810-193 Aveiro, Portugal
[3]Department of Electrical Engineering, University of Brasília (UnB), Brasília 70910-900, Brazil
[4]Institute for Advanced Studies in Communications (Iecom), Campina Grande 58109-970, Brazil
[5]Department of Communications Engineering, Federal University of Rio Grande do Norte (UFRN), Natal 59078-970, Brazil

Corresponding author: Higo Thaian P. Da Silva (higo.silva@ee.ufcg.edu.br)

This work was supported in part by the National Council for Science and Technology (CNPq), in part by the Coordination for the Improvement of Higher Education Personnel-Brazil (CAPES) under Grant 001; in part by CAPES—PROCAD-DEFESA and by the Foundation for Science and Technology, Ministry of Science, Technology and Higher Education of Portugal (FCT/MCTES), and co-funded by European Union (EU) Funds under Project UIDB/50008/2020-UIDP/50008/2020.

ABSTRACT Future wireless communication systems depend on the network's ultra-densification, on the application of massive multiple-input multiple-output (mMIMO) techniques and on the use of higher frequency bands to satisfy the ever-increasing demands for capacity. The operation of cell-free (CF) networks in the millimeter wave (mmWave) spectrum combines those principles, because they are composed of multiple access points (APs) distributed over a geographic region which serve a small number of users. Despite the extensive available bandwidth, the mmWave spectrum imposes high path losses and significant atmospheric molecular absorption to the links. In addition, in this frequency range, rain attenuation can notably degrade communications. Therefore, this article presents a study of the impact of rain attenuation on CF networks operating in the mmWave spectrum, this is in the 26 GHz, 38 GHz and 73 GHz frequency bands, based on site-specific ray tracing simulations. The propagation simulation is characterized under the effects of reflection, diffraction, diffuse scattering, atmospheric molecular absorption, vegetation losses and rain attenuation. The channel model is characterized using a hybrid approach, with the large-scale parameters determined by ray tracing in an environment subject to random Rician small-scale fading. The system performance is measured by the sum spectral efficiency (SSE) and energy efficiency (EE). According to the results, it was observed that AP densification protects the network against the effect of rain attenuation. Furthermore, even in sparse networks, the CF system has low sensitivity with respect to the precipitation rate, resulting in relatively small reductions in the average SSE and EE.

INDEX TERMS Cell-free, energy efficiency, massive MIMO, millimeter wave, rain attenuation, ray tracing, spectral efficiency.

I. INTRODUCTION

Networks ultra densification, massive multiple-input multiple-output (mMIMO) and communications in the millimeter wave (mmWave) spectrum are key technologies to achieve the performance metrics of future wireless systems [1], [2], [3]. The so-called cell-free (CF) mMIMO networks have the potential to combine these three techniques. CF networks share characteristics of traditional cellular collocated mMIMO, such as the arrangement of a large

The associate editor coordinating the review of this manuscript and approving it for publication was Irfan Ahmed.

number of antennas, simple linear precoding and application of a time-division-duplexing (TDD) scheme [4]. However, CF networks break with the cellular paradigm, relying on a distributed architecture in which a large number of access points (APs), connected to a central processing unit (CPU), are distributed over a geographic region, serving a smaller number of users. It has been shown that this distributed architecture is capable of outperforming small-cell networks in terms of 95%-likely per-user throughput [5], [6], [7]. CF networks also outperform traditional co-located cellular systems in serving high-mobility terminals [8]. Furthermore, by utilizing optimal power control schemes, the CF system ensures a consistent quality of service across all users within its coverage area [9], [10].

Despite being originally proposed to operate in the sub-6 GHz band [5], [11], several works presented in the literature analyze CF networks with carriers in the mmWave band [12], [13], [14], [15], [16]. The mmWave spectrum comprises the bands between 30 GHz and 300 GHz [17], [18]. This frequency range has an extensive continuous bandwidth available for broadband applications which, depending on the coverage area, can exceed the entirety of the already congested sub-6 GHz spectrum by several orders of magnitude [2]. In addition, the short wavelength allows the packaging of a large number of antennas in a compact-sized array, enabling narrow beamwidths [19]. Regulatory institutions indicate that the bands around the frequencies of 28 GHz, 38 GHz and 73 GHz have the potential to be explored in outdoor microcellular applications [18], [20]. In Brazil, the National Telecommunications Agency (Anatel) suggests the use of the 26 GHz band in future mmWave communications [21].

Despite its extensive available bandwidth, communications in the mmWave spectrum suffer from high path losses and attenuation by atmospheric molecular absorption. In addition, they are more susceptible to attenuation induced by vegetation and rain [18]. Rainfall attenuation significantly impacts communications operating above 10 GHz [22]. In the mmWave range, the wavelength varies between 10 mm and 1 mm, which is comparable in order of magnitude to the diameter of raindrops. In this regime, the interaction of the propagating electromagnetic wave with the raindrops is determined by energy absorption and scattering, which result in attenuation, [22], [23], [24]. Wave attenuation in a medium with a random distribution of raindrops depends on the characteristics of the transmitted signal, such as frequency and wave polarization, as well as on the properties of the rain, such as the drop size distribution (DSD) and the rain rate [23]. An analytical solution for rain attenuation can be calculated from Mie scattering theory, which applies the DSD to define the rain specific attenuation (dB/km) [25]. However, other methods with lower computational cost can be used for this purpose, such as the widely applied empirical model provided in the recommendation ITU-R 838-3 [26]. As an advantage, this model allows the calculation of the specific rain attenuation through a numerically simple expression, without depending on the local DSD.

Considering the importance of CF networks operating in the mmWave spectrum, the impact of rain attenuation on key performance metrics, such as spectral efficiency (SE) and energy efficiency (EE), needs to be investigated. To the best of authors knowledge, the effect of rain attenuation on CF networks has only been investigated in [16]. The mentioned work evaluates the influence of rainfall attenuation on the average SE in an environment with low urban density. However, the assessment only considers one fixed network configuration with a predetermined number of APs, which neglects the impact of varying AP density on the coverage area. Additionally, the study neither provides an analysis using rainfall exceedance probability as indicator nor explores the impact of rainfall attenuation on the average EE.

Therefore, this work presents a study of the impact of rain attenuation on the SE and EE of CF networks operating in the mmWave spectrum. A hybrid methodology has been applied, which combined the ray tracing deterministic method, used to characterize the channel large-scale parameters, with a random small-scale fading model [16], [27]. The site-specific three-dimensional ray tracing model is based on the shooting-and-bouncing rays (SBR) method and consider the effects of reflection, diffraction, diffuse scattering, atmospheric molecular absorption, foliage attenuation and rain attenuation. The propagation environment model applied in the simulations is based on mapping regions of the city of São Paulo, Brazil. In this work, CF networks with multi-antenna APs operating at 26 GHz, 38 GHz and 73 GHz under the effect of rain regimes with a maximum rate of 100 mm/hour are simulated. Although statistical and empirical channel models are capable of specifying several characteristics of multipath behavior [28], [29], they tend to generalize and abstract electromagnetic propagation while assuming certain aspects about the channel that may not be universally applicable. In contrast, this study evaluates CF networks by means of real-data ray tracing simulations applied to environments models comparable to typical urban settings. This methodology enables an accurate evaluation of the impact of different factors on the links [30], [31], which is crucial for designing local CF network projects [16], [27].

Based on the simulation results, this study presents significant findings on channel modeling and performance of CF networks under the effect of rain attenuation. The results of the channel modeling show the determination of various large-scale parameters in the propagation environment, including the propagation exponent, standard deviation of the shadow fading, Rice factor, line-of-sight probability, root-mean-square delay spread and root-mean-square Doppler spread. In addition, the study evaluates the impact of rain attenuation on the statistics of these parameters across precipitation rates ranging from 0 mm/hour to 100 mm/hour. The statistical characterization of the rain attenuation factor in the aforementioned frequencies is also presented. In order

to assess the performance of CF networks, we calculate the average sum spectral efficiency (SSE) and EE. This paper is the first to present an evaluation of the EE of CF networks by means of ray tracing based channel characterization. An investigation on the impact of rain attenuation on the performance metrics is presented, which compares the results to a scenario with no rain. The simulations reveal an unprecedented empirical expression for the relationship between the average SSE and EE and rainfall rate. Using this expression it is possible to quantify the average rate of change of these metrics as the precipitation increases. Additionally, the impact of attenuation on performance metrics is evaluated under different rainfall exceedance rates.

A. PAPER ORGANIZATION

The rest of this paper is organized as follows. In Section II, the CF system adopted in this work is described. Then, in Section III, the ray tracing main specificities are exposed, including the rain attenuation and channel modeling and the description of the propagation environment. In Section IV, the numerical results are presented and discussed. Finally, in Section V, the conclusions are presented.

B. NOTATION

Boldface uppercase and lowercase symbols denote matrices and columns vectors, respectively. The $N \times N$ identity matrix is written as $\mathbf{I}_N$. The Euclidean norm of a vector $\mathbf{v}$ is denoted as $\|\mathbf{v}\|$. The n-th element of a column vector $\mathbf{v}$ is denoted as $[\mathbf{v}]_n$. The superscripts $(\cdot)^*$, $(\cdot)^T$ and $(\cdot)^H$ represent the conjugate, the transpose and the conjugate-transpose, respectively. The trace of a matrix $\mathbf{A}$ is denoted as $\mathrm{tr}(\mathbf{A})$. The expected value operator is written as $\mathbb{E}[\cdot]$. An arbitrary complex Gaussian random vector $\mathbf{z}$, with mean vector $\boldsymbol{\mu}$ and covariance matrix $\boldsymbol{\Sigma}$, is denoted as $\mathbf{z} \sim \mathcal{CN}(\boldsymbol{\mu}, \boldsymbol{\Sigma})$. In turn, $\mathcal{LN}(\mu, \sigma)$ denotes the lognormal distribution with parameters μ and σ. Finally, $\mathbf{1}_{\mathcal{S}}(x)$ denotes the indicator function of an arbitrary subset $\mathcal{S}$, in which $\mathbf{1}_{\mathcal{S}}(x) = 1$ if $x \in \mathcal{S}$ and $\mathbf{1}_{\mathcal{S}}(x) = 0$ if $x \notin \mathcal{S}$.

II. CELL-FREE SYSTEM ANALYSIS

A. SYSTEM MODEL

The CF mMIMO system architecture, considered in this work, is illustrated in Fig. 1, in which M APs, each one equipped with an uniform linear array (ULA) of L antennas, are arranged in the sites serving K single-antenna user equipment (UE) consuming the same time-frequency resources [16], [32]. The channel gain vector between the m-th AP and the k-th UE, denoted as $\mathbf{g}_{m,k}$, is given by [16], [33]

$$\mathbf{g}_{m,k} = \sqrt{\beta_{m,k}} \left(\sqrt{\frac{F_{m,k}}{F_{m,k}+1}} \bar{\mathbf{h}}_{m,k} + \sqrt{\frac{1}{F_{m,k}+1}} \tilde{\mathbf{h}}_{m,k} \right), \quad (1)$$

in which $\beta_{m,k}$ represents the large-scale fading, that incorporates the effects of path losses, shadowing and rain attenuation; $F_{m,k}$ is the Rice factor, $\bar{\mathbf{h}}_{m,k}$ is the line-of-sight (LoS) components vector and $\tilde{\mathbf{h}}_{m,k} \sim \mathcal{CN}(\mathbf{0}, \mathbf{I}_L)$ is the small-scale fading vector. It should be mentioned that the small-scale fading components are assumed to be mutually uncorrelated. The large-scale fading can be rewritten as $\beta_{m,k} = \breve{\beta}_{m,k} \Omega_r$ [see Section III-C], in which $\breve{\beta}_{m,k}$ is the large-scale fading in a non-rainy scenario and Ω_r is the total rain attenuation.

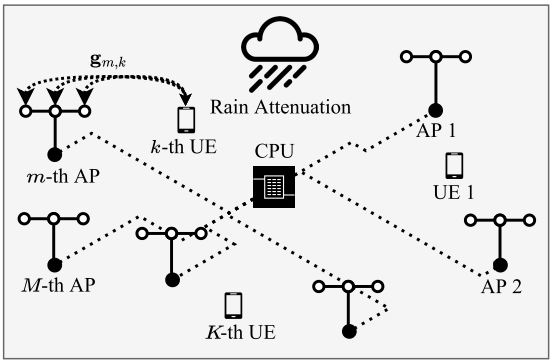

FIGURE 1. Cell-free mMIMO system.

The parameters $\beta_{m,k}$, $F_{m,k}$ and $\bar{\mathbf{h}}_{m,k}$ in (1) are determined from the ray tracing simulations. Thus, $\mathbf{g}_{m,k}$ can be decomposed into a deterministic vector, defined by ray tracing and denoted as $\bar{\mathbf{g}}_{m,k}$, and a random vector, written as $\tilde{\mathbf{g}}_{m,k}$. These vectors are described as

$$\bar{\mathbf{g}}_{m,k} = \sqrt{\frac{\beta_{m,k} F_{m,k}}{F_{m,k}+1}} \bar{\mathbf{h}}_{m,k} \quad (2)$$

and

$$\tilde{\mathbf{g}}_{m,k} = \sqrt{\frac{\beta_{m,k}}{F_{m,k}+1}} \tilde{\mathbf{h}}_{m,k}, \quad (3)$$

resulting in a channel vector $\mathbf{g}_{m,k} \sim \mathcal{CN}(\bar{\mathbf{g}}_{m,k}, \alpha_{m,k} \mathbf{I}_L)$, with $\alpha_{m,k} = \beta_{m,k}/(F_{m,k}+1)$ [16].

Assuming that the CF network operates with a TDD scheme, a coherence block that supports τ_c samples is subdivided into a training phase of length $\tau_p < \tau_c$, in which pilot sequences are transmitted for channel estimation, and a downlink data transmission phase of length $\tau_d = \tau_c - \tau_p$. As in [16], the coherence block length is determined from the ray tracing simulations, calculating $\tau_c = \min\left(B_{c;m,k} \times T_{c;m,k}\right), \forall\ (m,k) \in \{1,\ldots,M\} \times \{1,\ldots,K\}$, in which $B_{c;m,k}$ is the coherence band and $T_{c;m,k}$ is the coherence time, both relative to the link between the m-th AP and the k-th UE. This methodology ensures that all transmissions occur within the coherence times of all network users [16].

The large-scale parameters are assumed to be approximately constant over several coherence blocks and known a priori [5]. This statement is also valid for rain attenuation. Applying the model presented in [34], one can calculate the probability of occurrence of rainy fading events for a duration τ_r longer than T_r, for a given attenuation threshold Ω_{th}, *i.e.*, the conditional probability $\mathrm{P}(\tau_r > T_r | \Omega_r > \Omega_{th})$. In Fig. 2, curves for the rain fade duration probability at 26 GHz are

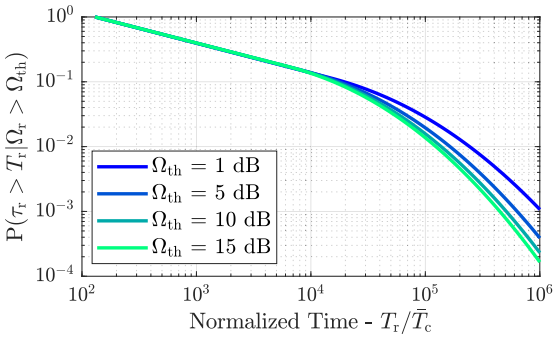

FIGURE 2. Rainfall attenuation exceedance probability for a time greater than T_r normalized to a coherence time of 7.6 ms.

presented with the abscissa axis normalized to a coherence time $\bar{T}_c = 7.2$ ms[1] for different values of Ω_{th}. It can be seen that rain fading has a high probability of exceeding Ω_{th} during hundreds or thousands coherence times. Therefore, it is reasonable to assume that rain attenuation remains approximately constant over multiple coherence blocks in the TDD scheme. Based on this observation, it is valid to state that $\beta_{m,k}$ is approximately constant during multiple coherence blocks even in rainy environments, given that rain induces slow fading.

B. UPLINK TRAINING PHASE

In the training phase, all K users transmit pilot sequences of length τ_p to all APs in the CF network. Denoting the pilot sequence transmitted by the k-th user as $\sqrt{\tau_p}\boldsymbol{\varphi}_k \in \mathbb{C}^{\tau_p \times 1}$, in which $\|\boldsymbol{\varphi}_k\|^2 = 1$ and $\boldsymbol{\varphi}_{k'}^H \boldsymbol{\varphi}_k \in \{0, 1\}, k' \neq k$, the matrix of received pilot sequences at the m-th AP, of order $L \times \tau_p$, can be written as [16], [35]

$$\mathbf{Y}_{p;m} = \sqrt{\tau_p P_p} \sum_{k=1}^{K} \mathbf{g}_{m,k} \boldsymbol{\varphi}_k^H + \mathbf{N}_{p;m}, \tag{4}$$

with P_p denoting the uplink transmitted power and $\mathbf{N}_{p;m}$ is the noise matrix at the m-th AP whose elements are independent and identically distributed (i.i.d.) $\mathcal{CN}(0, \sigma_{AP}^2)$ random variables. The APs estimate the channel vectors based on the projections of $\mathbf{Y}_{p;m}$ on $\boldsymbol{\varphi}_k$, calculated as [16]

$$\mathbf{y}_{m,k} = \underbrace{\sqrt{\tau_p P_p}\mathbf{g}_{m,k}}_{\text{Channel}} + \underbrace{\sqrt{\tau_p P_p} \sum_{k' \neq k}^{K} \mathbf{g}_{m,k'} \boldsymbol{\varphi}_{k'}^H \boldsymbol{\varphi}_k}_{\text{Pilot Contamination}} + \underbrace{\tilde{\mathbf{n}}_{p;m,k}}_{\text{Noise}}, \tag{5}$$

in which $\tilde{\mathbf{n}}_{p;m,k} = \mathbf{N}_{p;m}\boldsymbol{\varphi}_k \sim \mathcal{CN}(\mathbf{0}, \sigma_{AP}^2 \mathbf{I}_L)$ is the equivalent noise vector. As highlighted in (5), the $\mathbf{y}_{m,k}$ vector can be decomposed into three parts: channel, pilot contamination and noise.

The projection vector $\mathbf{y}_{m,k}$ can be rewritten as $\mathbf{y}_{m,k} = \bar{\mathbf{y}}_{m,k} + \tilde{\mathbf{y}}_{m,k}$, with $\bar{\mathbf{y}}_{m,k}$ and $\tilde{\mathbf{y}}_{m,k}$ denoting the deterministic (result of ray tracing simulations) and random parts, respectively, in which [16]

$$\bar{\mathbf{y}}_{m,k} = \sqrt{\tau_p P_p}\bar{\mathbf{g}}_{m,k} + \sqrt{\tau_p P_p} \sum_{k' \neq k}^{K} \bar{\mathbf{g}}_{m,k'} \boldsymbol{\varphi}_{k'}^H \boldsymbol{\varphi}_k \tag{6}$$

and

$$\tilde{\mathbf{y}}_{m,k} = \sqrt{\tau_p P_p}\tilde{\mathbf{g}}_{m,k} + \sqrt{\tau_p P_p} \sum_{k' \neq k}^{K} \tilde{\mathbf{g}}_{m,k'} \boldsymbol{\varphi}_{k'}^H \boldsymbol{\varphi}_k + \tilde{\mathbf{n}}_{p;m,k}. \tag{7}$$

Based on $\tilde{\mathbf{y}}_{m,k} = \mathbf{y}_{m,k} - \bar{\mathbf{y}}_{m,k}$, each AP computes a Bayesian minimum mean square error (MMSE) estimation, determining the estimated channel vector by [36]

$$\hat{\mathbf{g}}_{m,k} = \bar{\mathbf{g}}_{m,k} + \left(\mathbb{E}\left[\tilde{\mathbf{g}}_{m,k}\tilde{\mathbf{y}}_{m,k}^H\right]\right)\left(\mathbb{E}\left[\tilde{\mathbf{y}}_{m,k}\tilde{\mathbf{y}}_{m,k}^H\right]^{-1}\right)\tilde{\mathbf{y}}_{m,k}. \tag{8}$$

It is possible to demonstrate that $\hat{\mathbf{g}}_{m,k} = \bar{\mathbf{g}}_{m,k} + c_{m,k}\tilde{\mathbf{y}}_{m,k}$, in which [33]

$$c_{m,k} = \frac{\sqrt{\tau_p P_p}\alpha_{m,k}}{\tau_p P_p \sum_{k' \in \mathcal{P}_k} \alpha_{m,k'} + \sigma_{AP}^2}, \tag{9}$$

with $\mathcal{P}_k = \{k' \in \{1, \ldots, K\} : \boldsymbol{\varphi}_{k'}^H \boldsymbol{\varphi}_k = 1\}$ denoting the subset of indexes of the users that apply the k-th pilot sequence. Therefore, the estimated channel vectors are distributed as $\hat{\mathbf{g}}_{m,k} \sim \mathcal{CN}(\bar{\mathbf{g}}_{m,k}, \gamma_{m,k}\mathbf{I}_L)$ and the estimation error, $\epsilon_{m,k} \triangleq \mathbf{g}_{m,k} - \hat{\mathbf{g}}_{m,k}$, is distributed as $\epsilon_{m,k} \sim \mathcal{CN}(\mathbf{0}, (\alpha_{m,k} - \gamma_{m,k})\mathbf{I}_L)$, in which [33]

$$\gamma_{m,k} = \frac{\tau_p P_p \alpha_{m,k}^2}{\tau_p P_p \sum_{k' \in \mathcal{P}_k} \alpha_{m,k'} + \sigma_{AP}^2}. \tag{10}$$

The allocation of mutually orthogonal pilot sequences to all users depends on the restrictions imposed by the channel regarding the coherence parameters. In the case where it is feasible to allocate $\tau_p > K$ samples in the TDD block of τ_c samples, it is possible to associate mutually orthogonal pilot sequences to all K users. In this case, the pilot contamination term in (5) disappears and $\mathcal{P}_k = \{k\}$ [16]. Otherwise, the reuse of pilot sequences becomes necessary, and the effect of pilot contamination is inherent in the channel estimation.

C. DOWNLINK DATA TRANSMISSION PHASE

Assuming conjugate beamforming precoding, the downlink transmitted signal by the m-th AP is described as [16], [35]

$$\mathbf{x}_m = \sqrt{P_d} \sum_{k=1}^{K} \sqrt{\eta_{m,k}}\hat{\mathbf{g}}_{m,k}^* q_k, \tag{11}$$

in which P_d is the downlink average power, $\eta_{m,k}$ are the power control coefficients and $q_k \sim \mathcal{CN}(0, 1)$ is the data symbol intended to the k-th user [37]. The APs are assumed

[1]Estimated value approximating the coherence time as the inverse of the maximum Doppler shift at 26 GHz observed by a pedestrian user at 1.6 m/s.

to transmit at full power ($\mathbb{E}\left[\|\mathbf{x}_m\|^2\right] = P_\mathrm{d}$) and based on that, the power control coefficients must satisfy the condition [32]

$$\sum_{k=1}^{K} \eta_{m,k}[\bar{\mathbf{g}}_{m,k}^H \bar{\mathbf{g}}_{m,k} + \mathrm{tr}(\gamma_{m,k}\mathbf{I}_L)] = 1. \tag{12}$$

To define the values of $\eta_{m,k}$, the simplest power allocation strategy is adopted, in which each AP allocates the same power to all network users. In this way, the power control coefficients are [16]

$$\eta_{m,k} = \left[L \sum_{k'=1}^{K} (\alpha_{m,k'} F_{m,k'} + \gamma_{m,k'}) \right]^{-1}. \tag{13}$$

Based on the assumptions of channel reciprocity in the TDD blocks and that each UE is only aware of the channel statistics, the signal received by the k-th user can be expressed by [38]

$$\begin{aligned} r_k &= \sum_{m=1}^{M} \mathbf{g}_{m,k}^T \mathbf{x}_m + n_{\mathrm{u};k} \\ &= \mathrm{DS}_k \cdot q_k + \mathrm{BU}_k \cdot q_k + \sum_{k' \neq k}^{K} \mathrm{UI}_{k,k'} \cdot q_{k'} + n_{\mathrm{u};k}, \end{aligned} \tag{14}$$

in which $n_{\mathrm{u};k} \sim \mathcal{CN}(0, \sigma_\mathrm{u}^2)$ is the noise at the k-th UE, DS_k is the desired signal, BU_k is the beamforming uncertainty and $\mathrm{UI}_{k,k'}$ is the k'-th user's interference on the k-th user's link. These terms are written as [16], [38]

$$\mathrm{DS}_k = \sqrt{P_\mathrm{d}} \mathbb{E}\left[\sum_{m=1}^{M} \sqrt{\eta_{m,k}} \mathbf{g}_{m,k}^T \hat{\mathbf{g}}_{m,k}^* \right], \tag{15}$$

$$\mathrm{BU}_k = \sqrt{P_\mathrm{d}} \sum_{m=1}^{M} \sqrt{\eta_{m,k}} \left(\mathbf{g}_{m,k}^T \hat{\mathbf{g}}_{m,k}^* - \mathbb{E}\left[\mathbf{g}_{m,k}^T \hat{\mathbf{g}}_{m,k}^* \right] \right) \tag{16}$$

and

$$\mathrm{UI}_{k,k'} = \sqrt{P_\mathrm{d}} \sum_{m=1}^{M} \sqrt{\eta_{m,k'}} \mathbf{g}_{m,k}^T \hat{\mathbf{g}}_{m,k'}^*. \tag{17}$$

D. SPECTRAL AND ENERGY EFFICIENCIES

Treating the sum of terms $\mathrm{BU}_k \cdot q_k + \sum_{k' \neq k}^{K} \mathrm{UI}_{k,k'} \cdot q_{k'} + n_{\mathrm{u};k}$ as effective noise and assuming that q_k is independent and uncorrelated of the terms in (14), one can calculate the signal-to-interference-plus-noise ratio (SINR) experienced by the k-th user using (18), as shown at the bottom of the next page, (see [16, Appendix A]), in which $\Lambda_{m,k,k'} = \gamma_{m,k'} \frac{\alpha_{m,k}}{\alpha_{m,k'}}$ is an auxiliary variable. The spectral efficiency (SE) experienced by the k-th user, denoted as S_k, is found by substituting (18) into [16]

$$S_k = (1 - \tau_\mathrm{p}/\tau_\mathrm{c}) \log_2(1 + \mathrm{SINR}_k). \tag{19}$$

The CF downlink sum SE (SSE), denoted as S_CF, is calculated by [32] and [39]

$$\begin{aligned} S_\mathrm{CF} &= \left(1 - \frac{\tau_\mathrm{p}}{\tau_\mathrm{c}}\right) \sum_{k=1}^{K} \log_2(1 + \mathrm{SINR}_k) \\ &= \left(1 - \frac{\tau_\mathrm{p}}{\tau_\mathrm{c}}\right) \log_2 \left(\prod_{k=1}^{K} \Upsilon_k \right), \end{aligned} \tag{20}$$

in which $\Upsilon_k = 1 + \mathrm{SINR}_k$.

Applying the CF mMIMO power consumption model presented in [32] and [39] and denoting the system bandwidth as B, the total consumed power in the network is expressed by

$$\begin{aligned} P_\mathrm{CF} = P_\mathrm{d} L \sum_{m=1}^{M} \sum_{k=1}^{K} \frac{1}{a_m} \eta_{m,k} (\alpha_{m,k} F_{m,k} + \gamma_{m,k}) \\ + \sum_{m=1}^{M} (L P_{\mathrm{tc};m} + P_{0;m}) + B \left(\sum_{m=1}^{M} \rho_{\mathrm{bt};m} \right) S_\mathrm{CF}, \end{aligned} \tag{21}$$

in which $0 < a_m \leq 1$ is the power amplifier efficiency, $P_{\mathrm{tc};m}$ is the power consumed by the antennas internal circuits, $P_{0;m}$ is the fixed power consumption of each backhaul link and ρ_bt is the traffic-dependent power (expressed in W/bits/s) related to the m-th AP [32], [39]. The CF mMIMO energy efficiency (EE), expressed in bits/J, is the ratio between the sum throughput (sum SE $\times$ bandwidth) and the total consumed power [32], [39], that is,

$$E_\mathrm{CF} = \frac{B \cdot S_\mathrm{CF}}{P_\mathrm{CF}}. \tag{22}$$

III. RAY TRACING MODELING

Applying the SBR method, the ray tracing algorithm is divided into three main stages: transmission, tracing and reception [16], [30], [40]. In the transmission stage, multiple rays are launched along the angular sphere from a given source point. To ensure that the rays have an uniform power density in an isotropic transmission, their distribution must be homogeneous per unit solid angle. In this case, the angle between adjacent rays is a constant, denoted as $\Delta\theta$ [40]. To acquire this ray uniformity, the transmitted rays are oriented to the vertices of an icosphere, defined as a geodesic polyhedron with vertices projected onto a sphere [31], [41].

The analysis scene, defined as the portion of the propagation environment considered for simulation, is subdivided into cubes of equal volume called voxels. In the tracing stage, the length of a ray is gradually increased along the voxels [42]. At each incremental step, the algorithm evaluates whether the ray interacts with objects within the boundaries of the current voxel. If an interaction occurs, the ray is reflected according to Snell's law and new ray sources can be generated to characterize diffractions or diffuse scatterings [43]. Finally, in the reception stage, spheres are delimited around the observation points and if a ray intercepts a particular sphere, its contribution is incorporated in the respective channel impulse response (CIR) [31].

An arbitrary received ray contributes to the CIR with a normalized power described by [16]

$$p_{\mathrm{r}} = \left(\frac{\lambda}{4\pi}\right)^2 \cdot A_{\mathrm{fs}} \cdot \rho_{\mathrm{p}} \cdot 10^{-\frac{\rho_m+\rho_f+\rho_r}{10}} \times \left(\prod_i A_{\mathrm{re};i}\Gamma_{\mathrm{i}}^2\rho_{\mathrm{ds};i}^2\right)\left(\prod_j A_{\mathrm{d};j}D_j^2\right)\left(\prod_k A_{\mathrm{ds};k}\zeta_k^2\right), \tag{23}$$

in which λ is the wavelength and A_{fs} is the free-space spread factor. The parameters ρ_{p}, ρ_{m}, ρ_{f} and ρ_{r} are loss factors induced by polarization mismatch [44], atmospheric molecular absorption, vegetation and rain, respectively. The frequency dependent atmospheric molecular absorption loss factor (ρ_{m}) is calculated according to the model presented in the recommendation ITU-R P.676 and incorporates the losses caused by dry air and water vapor [45]. The foliage induced losses (ρ_{f}), caused by absorptions and scatterings in the vegetation medium, are calculated using the ITU-R slant path model [46], [47]. The determination of the rain attenuation factor (ρ_{r}) is detailed in Section III-A.

In sequence, considering a reflective interaction on a rough surface of effective roughness σ_{h}, the factors Γ_i^2 and ρ_s^2 in (23) denote the loss in the reflective interaction, calculated using Fresnel coefficients, and the excess loss in the specular direction due to diffuse scattering, respectively [48]. The D_j^2 value represents the diffraction loss and is found using the uniform theory of diffraction (UTD) [49], [50]. Based on the Beckmann-Kirchhoff theory, the ζ_k^2 factor characterizes diffuse scattering losses in an arbitrary direction [43], [48]. Finally, the terms $A_{\mathrm{re};i}$, $A_{\mathrm{d};j}$ and $A_{\mathrm{ds};k}$ refer to the spread factors of reflection, diffraction and diffuse scattering, respectively; which depend on the lengths of the paths involved in each phenomenon [48], [51].

A. RAIN ATTENUATION MODELING

To characterize the rainfall attenuation, different approaches, classified as empirical, statistical and physical, are presented in the literature [52], [53], [54]. In this work, we apply the empirical model presented in the recommendations ITU-R P.837 and ITU-R P.838 to predict the excess rainfall losses [26], [55]. According to this model, the specific attenuation, expressed in dB/km, is calculated by the power-law [26], [56]

$$\gamma_{\mathrm{r}} = k_{\mathrm{r}} C_{\mathrm{r}}^{a_{\mathrm{r}}}, \tag{24}$$

with C_{r} denoting the rainfall rate (mm/hour). In (24), k_{r} and a_{r} are parameters that depend on the frequency (f), polarization tilt angle (τ_{p}) and elevation angle (ϕ) of the path in the rainy medium [26]. The values of k_{r} and a_{r} are available in the lookup table exposed in [26].

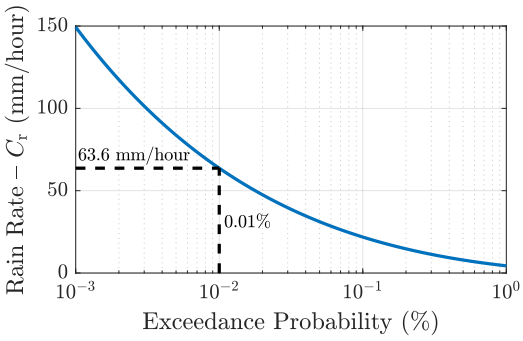

FIGURE 3. Rainfall rate versus percentage time of an average year in the simulated sites.

For a given location, it is possible to calculate the rainfall rate exceeded for a given percentage of time in an average year [55]. Fig. 3 presents the rainfall rate as a function of the respective exceedance probability for the location of the sites considered in the ray tracing simulations (see Table 1). As marked in the figure, in an average year, rainy events have a rate greater than 63.6 mm/hour in 0.01% of the time, *i.e.*, 99.9% of rainfall events have a rate less than or equal to 63.6 mm/hour. In the simulations, rains are considered with a maximum rate of 100 mm/hour (0.003% of exceedance).

Considering that the CF network analyzed in this work has short links, with a propagation environment with area of 500 m × 500 m, and that the rain cells tend to remain homogeneous over a few kilometers [57], it is assumed that the rainfall rate is constant along the rays paths. Based on this assumption, the rainfall attenuation (dB) is calculated by[2]

$$\rho_{\mathrm{r}} = \gamma_{\mathrm{r}} \ell_0. \tag{25}$$

[2]Frequently, in rain attenuation models, a reduction factor multiplied by ℓ_0 is considered to correct the effect of rain non-homogeneity along the path [58], [59]. However, this correction factor is only necessary for long links [60], where the inhomogeneity effect is evident.

$$\mathrm{SINR}_k = \frac{L^2\left|\sum_{m=1}^{M}\sqrt{\eta_{m,k}}(\gamma_{m,k}+\alpha_{m,k}F_{m,k})\right|^2}{L\sum_{k'=1}^{K}\sum_{m=1}^{M}\eta_{m,k'}\alpha_{m,k}(\gamma_{m,k'}F_{m,k}+\gamma_{m,k'}+\alpha_{m,k'}F_{m,k'})+\sum_{k'\neq k}^{K}\left|\sum_{m=1}^{M}\sqrt{\eta_{m,k'}}\left(\bar{\mathbf{g}}_{m,k}^T\bar{\mathbf{g}}_{m,k'}^*+\mathbf{1}_{\mathcal{P}_{k'}}(k)L\Lambda_{m,k,k'}\right)\right|^2+\frac{\sigma_{\mathrm{u}}^2}{P_{\mathrm{d}}}} \tag{18}$$

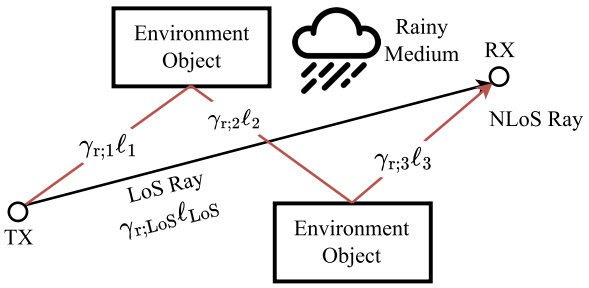

FIGURE 4. Rain attenuation on LoS and NLoS links.

in which ℓ_0 is the path length expressed in km. For LoS links, expressions (24) and (25) can be directly applied. However, the calculation of the rain attenuation in non-line-of-sight (NLoS) rays must consider the characteristics of each individual path [61]. For this, consider an arbitrary ray that is traced by N_p paths. Each path is characterized by a length ℓ_n, an elevation angle ϕ_n and a tilt polarization angle $\tau_{p;n}$, with $1 \leq n \leq N_p$. In this case, each path has a particular specific attenuation, denoted by $\gamma_{r;n}$, and the total attenuation experienced by this ray is calculated by

$$\rho_{r;t} = \sum_{n=1}^{N_p} \gamma_{r;n}\ell_n. \tag{26}$$

Fig. 4 illustrates the calculation of rain attenuation. The total rain attenuation on a link composed of many received rays, Ω_r, is discussed in Section III-C.

B. PROPAGATION ENVIRONMENT MODEL

The propagation environment model considered in the simulations is based on the mapping of part of the Cerqueira César and Jardim Paulista neighborhoods, close to Paulista Avenue, in São Paulo city, Brazil. The environment objects are modeled as polyhedrons, with base polygons and height profiles taken from OpenStreetMap and Google Earth [62]. A view of the propagation environment model is shown in Fig. 5.

These objects are classified as houses, buildings or vegetation, and each class has specific parameters to characterize interactions with rays. Objects representing vegetation are predefined, while the remaining objects are sorted according to their heights. Objects with a height of less than 7 m are classified as houses, otherwise they are considered buildings. It is assumed that the walls and roof planes of the houses are composed by bricks and roofing tiles, respectively. On the other hand, the entire surface of the buildings is made of concrete. The ground plane material throughout its area is asphalt. The values of electrical permittivity and effective roughness of the considered materials are found in [63], [64], [65], [66].

The simulations are performed in two different square sites of area $\ell_s \times \ell_s$. The central coordinates of each site are listed in Table 1. All sites are subdivided into N_{mr} square microregions of area $\ell_{mr} \times \ell_{mr}$, in which the receptor points

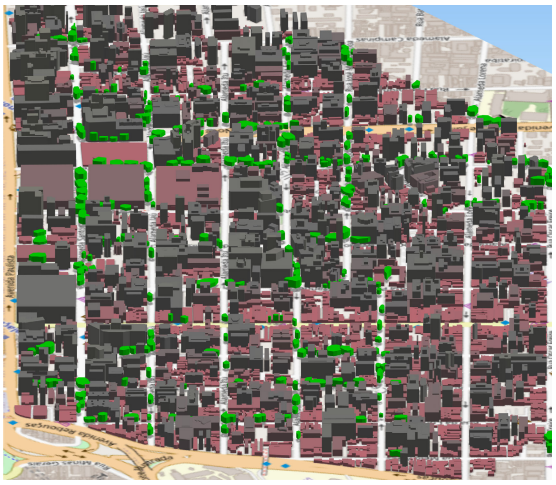

FIGURE 5. Propagation environment model.

TABLE 1. Central coordinates of the considered sites.

Site Index	Center Coordinate	
	Longitude	Latitude
1	46°39'47.5"W	23°33'44.2"S
2	46°39'29.9"W	23°33'44.4"S

are positioned in their centers at a height h_{UE}, composing a reception grid. In this grid, receiver points are indexed by a (i, j) pair. Receiver points contained within the boundaries of some object in the environment are discarded. Therefore, considering an area with N_{mr} microregions, there are $N_v < N_{mr}$ valid positions to allocate users.

A CF network ray tracing simulation with K users generates a dataset with only K SE samples, which is not enough to assemble statistics and analyze the system performance. To mitigate this limitation and avoid running multiple ray tracing simulations, which are computationally expensive, the user group method (UG) is applied [16], [27]. An UG is composed of K users who occupy K random positions in the reception grid. The total number of UGs per simulation is $N_{UG} = \lfloor N_v/K \rfloor$, with $\lfloor \cdot \rfloor$ denoting the floor function. There is no dependency or correlation between members of different UGs, that is, each individual set of M APs and an UG represents an individual case of CF network. In this configuration, the simulations generate $(M \times L) \times (K \times N_{UG})$ channel parameters, $K \times N_{UG}$ SE values and N_{UG} SSE and EE values.

The environment considered in the simulations can be classified as dense urban, containing blocks of buildings with heights up to 90 m (relative to the ground plane). Practical and efficient methodologies for deploying APs in mapping-based environments still need to be investigated. Frequently, in analyzes of CF networks, the APs are randomly distributed throughout the environment [10], [67], [68]. The application of this methodology in dense urban environments can allocate APs in completely obstructed regions, which can reduce the overall performance of the system. Therefore,

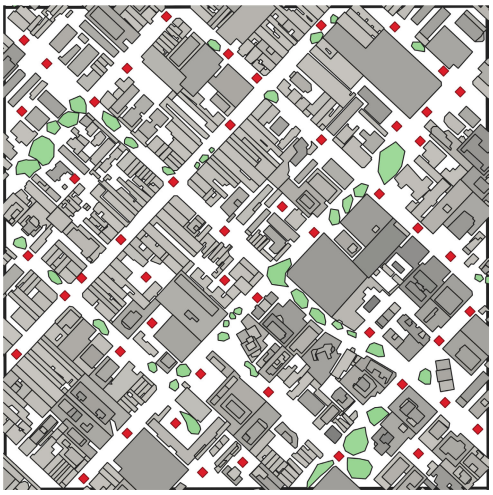

FIGURE 6. Arrangement of $M = 50$ APs (red dots) in an area of 500 m × 500 m.

assuming that the CF network must serve pedestrian users, in this work, the APs are arranged in predefined positions on the streets bordered by the building blocks at a fixed height h_{AP}. Consequently, links are predominantly confined to street canyons. Fig. 6 illustrates the arrangement of $M = 50$ APs in an area of 500 m × 500 m in Site 1 (see Table 1).

C. RAY TRACING CHANNEL MODEL

The ray tracing simulations consider M APs, each one equipped with an ULA of L antennas, transmitting rays that are captured by $N_{\mathrm{UG}} \times K$ receiving points. Assuming that the minimum separation between antenna elements, denoted as d_{ant}, is equal to $d_{\mathrm{ant}} = \lambda/2$, the largest physical dimension of the ULAs is $D_{\mathrm{array}} = (L-1)\lambda/2$. To ensure that the receiving points are in the far-field region, delimited by the Rayleigh distance $d_{\mathrm{ff}} = 2D^2_{\mathrm{array}}/\lambda$ [69], we consider ULAs with a maximum of 64 antennas. In this case, the largest array, operating at 26 GHz, has a length equal to 0.36 m. Therefore, it is valid to assume that all antennas of the same AP share the same large-scale parameters, given that these parameters remain strongly correlated in a spacement of a few meters [70]. Based on this assumption, it is not necessary to transmit rays from all antenna elements, which would result in redundancy and high computational cost. Therefore, in the simulations, the rays are emitted from the centroids of each ULA, and not from the individual positions of each antenna element.

Consider the ULA of the m-th AP, where the position of the l-th antenna element is given by [16]

$$\mathbf{e}_{m,l} = \mathbf{c}_m + \frac{\lambda}{2}\left[l - \left(\frac{L+1}{2}\right)\right]\mathbf{t}_m, \tag{27}$$

with $\mathbf{c}_m$ denoting the ULA centroid position vector and $\mathbf{t}_m$ denoting the array orientation unit vector. In this configuration, the elements of the LoS vector are calculated by [16]

$$[\bar{\mathbf{h}}_{m,k}]_l = \exp\left\{-j\frac{2\pi}{\lambda}d_{\mathrm{ant}}\left[l - \left(\frac{L+1}{2}\right)\right]\cos(\bar{\phi}_{m,k})\right\}, \tag{28}$$

in which $\bar{\phi}_{m,k}$ is the angle between $\mathbf{t}_m$ and the LoS ray [16].

Assuming that the link between the m-th AP and the k-th user is composed by a superposition of $N_{\mathrm{r};m,k}$ rays, the respective CIR is described as [16]

$$H_{m,k}(t,\tau,\Theta,\Phi) = \sum_{n=1}^{N_{\mathrm{r};m,k}} \sqrt{p_{\mathrm{r};m,k,n}}e^{-j\varphi_{m,k,n}(t)}\delta(\tau-\tau_{m,k,n}) \times \delta(\Theta-\Theta_{m,k,n})\delta(\Phi-\Phi_{m,k,n}), \tag{29}$$

in which t, τ, Φ and Θ denote the absolute time, delay, angle of arrival (AoA) and angle of departure (AoD) domains, respectively. In turn, $p_{\mathrm{r};m,k,n}$ is the normalized power, calculated by means of (23), and $\tau_{m,k,n}$ is the delay of the n-th received ray. In the angle domains, $\Theta_{m,k,n} = [\theta_{\mathrm{a};m,k,n}, \phi_{\mathrm{a};m,k,n}]^T$ and $\Phi_{m,k,n} = [\theta_{\mathrm{d};m,k,n}, \phi_{\mathrm{d};m,k,n}]^T$ are the AoA and AoD vectors, respectively, with $(\theta_{\mathrm{a};m,k,n}, \theta_{\mathrm{d};m,k,n})$ expressing azimuth angles and $(\phi_{\mathrm{a};m,k,n}, \phi_{\mathrm{d};m,k,n})$ expressing elevation angles. In sequence, $\varphi_{m,k,n}(t)$ is the phase component of the n-th received ray, described by [71]

$$\varphi_{m,k,n}(t) = 2\pi[(f+\nu_{m,k,n})\tau_{m,k,n} - \nu_{m,k,n}t], \tag{30}$$

in which $\nu_{m,k,n}$ is the Doppler shift, given by [70]

$$\nu_{m,k,n} = \frac{1}{\lambda}\mathbf{v}_k \cdot \mathbf{k}_{m,k,n}, \tag{31}$$

with $\mathbf{k}_{m,k,n}$ representing the direction vector of the received ray and $\mathbf{v}_k$ denoting the instantaneous velocity vector of the k-th user with random direction and norm equal to $\|\mathbf{v}_k\| = \nu_{\mathrm{UE}}$, in which ν_{UE} is the user scalar velocity.[3]

Based on the CIR in (29), it can be shown that the joint power spectrum of the channel, written as $P_{m,k}(\nu,\tau,\Theta,\Phi)$, with ν denoting the Doppler shift domain, is given by [16]

$$P_{m,k}(\nu,\tau,\Theta,\Phi) = \sum_{n=1}^{N_{\mathrm{r};m,k}} p_{\mathrm{r};m,k,n}\delta(\tau-\tau_{m,k,n})\delta(\nu-\nu_{m,k,n}) \times \delta(\Theta-\Theta_{m,k,n})\delta(\Phi-\Phi_{m,k,n}). \tag{32}$$

The marginal power spectra can be found by integrating (32) in the remaining domains and respective supports. To characterize the communication channel, the large-scale fading, shadow fading, Rice factor, root-mean-square delay spread (RMS-DS) and root-mean-square Doppler spread (RMS-DoS) are extracted from (32).

The channel gain, which characterizes large-scale fading, is calculated by [16]

$$\beta_{m,k} = \sum_{n=1}^{N_{\mathrm{r};m,k}} p_{\mathrm{r};m,k,n}. \tag{33}$$

[3] It is assumed that the velocity vectors do not change their direction during the reception of all multipath components and that there is no significant position variation within a coherence time.

Analyzing the expression in (23), it can be seen that the power of the received ray depends on the attenuation by rain ρ_{r} in a given rainy regime with rate C_{r}. Therefore, denoting the received rays powers as a function of the rainfall rate by $p_{\mathrm{r};m,k,n}(C_{\mathrm{r}})$, one can rewrite the value of $\beta_{m,k}$ as

$$\beta_{m,k} \triangleq \beta_{m,k}(C_{\mathrm{r}}) = \sum_{n=1}^{N_{\mathrm{r};m,k}} p_{\mathrm{r};m,k,n}(C_{\mathrm{r}}) = \breve{\beta}_{m,k}\Omega_{\mathrm{r}}(C_{\mathrm{r}}), \quad (34)$$

in which $\breve{\beta}_{m,k}$ is large-scale fading in the absence of rain, i.e., $\beta_{m,k}(0) = \breve{\beta}_{m,k}$, and $\Omega_{\mathrm{r}}(C_{\mathrm{r}}) \leq 1$ is the rain total attenuation. The latter parameter is calculated by

$$\Omega_{\mathrm{r}}(C_{\mathrm{r}}) = \frac{\sum_{n=1}^{N_{\mathrm{r};m,k}} p_{\mathrm{r};m,k,n}(C_{\mathrm{r}})}{\sum_{n=1}^{N_{\mathrm{r};m,k}} p_{\mathrm{r};m,k,n}(0)}. \quad (35)$$

In statistical models, the term $\Omega_{\mathrm{r}}(C_{\mathrm{r}})$ is characterized by a log-normal random variable of mean μ_{Ω} and standard deviation σ_{Ω} [72].

Using the $\beta_{m,k}$ data and applying the close-in free-space (CI) model [73], the average distance-dependent path losses can be characterized by

$$\mathrm{PL}_{\mathrm{CI}}(f, d_{\mathrm{tx}}; \kappa) = \mathrm{PL}_{\mathrm{FS}}(f, d_0) + 10\kappa \log_{10}(d_{\mathrm{tx}}), \quad (36)$$

in which $d_{\mathrm{tx}} > d_0$ is the distance between the transmitter and the received, κ is the propagation exponent and $\mathrm{PL}_{\mathrm{FS}}(f, d_0)$ is the free-space path loss at a reference distance d_0, which is considered $d_0 = 1$ m. The parameter κ is found by a linear least square regression. In turn, the link shadow fading is given by

$$\chi_{m,k} = 10\log_{10}(\beta_{m,k}) - \mathrm{PL}_{\mathrm{CI}}(f, d_{m,k}; \kappa), \quad (37)$$

in which $d_{m,k}$ denote the distance between the m-th AP and the k-th user. The link shadow fading is parameterized by its sample standard deviation σ_{χ}.

The Rice factor, defined as the ratio between the LoS power and the remaining scattered power, is found by [16]

$$F_{m,k} = \frac{\bar{p}_{m,k}}{\beta_{m,k} - \bar{p}_{m,k}}, \quad (38)$$

with $\bar{p}_{m,k}$ denoting the LoS ray power. Using the data obtained in simulation, referring to the users LoS condition, and applying the model presented in [73], it is possible to characterize the distance-dependent LoS probability by [73]

$$p_{\mathrm{LoS}}(d_{\mathrm{tx}}) = \min\left(\frac{d_1}{d_{\mathrm{tx}}}, 1\right)\left(1 - e^{-\frac{d_{\mathrm{tx}}}{d_2}}\right) + e^{-\frac{d_{\mathrm{tx}}}{d_2}}, \quad (39)$$

in which d_1 and d_2 are fit parameters that can be found by a mean square error minimization.

Temporal and spectral dispersions are respectively provided by the RMS-DS $\sigma_{\tau;m,k}$ and the RMS-DoS $\sigma_{\nu;m,k}$, in which [16]

$$\sigma_{\tau;m,k} = \sqrt{\frac{1}{\beta_{m,k}} \sum_{n=1}^{N_{\mathrm{r};m,k}} p_{\mathrm{r};m,k,n}(\tau_{m,k,n} - \mu_{\tau;m,k})^2}, \quad (40)$$

$$\sigma_{\nu;m,k} = \sqrt{\frac{1}{\beta_{m,k}} \sum_{n=1}^{N_{\mathrm{r};m,k}} p_{\mathrm{r};m,k,n}(\nu_{m,k,n} - \mu_{\nu;m,k})^2}, \quad (41)$$

with $\mu_{\tau;m,k}$ and $\mu_{\nu;m,k}$ denoting the mean delay and the mean Doppler shift, respectively. To calculate the coherence band and coherence time, the approximations $B_{\mathrm{c};m,k} \approx 1/(50\sigma_{\tau;m,k})$ and $T_{\mathrm{c};m,k} \approx 1/\sigma_{\nu;m,k}$ are applied [74].

IV. NUMERICAL RESULTS

This section presents the main results of the ray tracing simulations. CF networks operating at 26 GHz, 38 GHz and 73 GHz are evaluated, considering sites with an area equal to 500 m × 500 m ($\ell_{\mathrm{s}} = 500$ m). The effect of interference from external APs to the simulated sites is not considered. The APs centroids are located at a height of $h_{\mathrm{AP}} = 15$ m, while the UEs are positioned in the reception grid at a height of $h_{\mathrm{UE}} = 1.5$ m. A slow mobility scenario is assumed, in which users move at a speed of $v_{\mathrm{UE}} = 1.6$ m/s. The ray tracing simulations are performed with an angular resolution equal to $\Delta\theta = 0.135°$. In addition, the ray paths are restricted to seven reflections. The links rain attenuations are calculated assuming that the rainfall rate is homogeneous throughout the propagation environment. Furthermore, it is assumed that the rainfall rate and attenuation do not vary across multiple coherence blocks. The simulations are proposed to show the effect of rain attenuation on the performance metrics of the CF network.

The evaluated CF networks are composed of a maximum of $M = 50$ APs, resulting in a density of 200 APs/km^2, serving at most $K = 15$ users. The link polarization is vertical-vertical, with a downlink average power $P_{\mathrm{d}} = 200$ mW and an uplink power $P_{\mathrm{p}} = 100$ mW. It is assumed that the APs and UEs have a noise figure equal to 6 dB and that the additive noise has a power spectral density equal to -174 dBm/Hz. The system bandwidth is considered $B = 20$ MHz. The power consumption parameters are $a_m = 0.4$, $P_{\mathrm{tc};m} = 0.2$ W, $P_{0;m} = 0.825$ W and $\rho_{\mathrm{bt};m} = 0.25$ W/Gbits/s [39]. Table 2 summarizes the simulation parameters.

A. CHANNEL MODELING RESULTS

This subsection presents the channel characterization results. For each carrier, the channel parameters and their respective statistics are extracted from data produced by simulation at the two specified sites. The results for non-rainy scenarios are summarized in Table 3. To measure the effect of rainy attenuation on the channel parameters and statistics, it is defined the factor $D_X(C_{\mathrm{r}}) \triangleq X(C_{\mathrm{r}}) - X(0)$, in which $X(C_{\mathrm{r}})$ is an arbitrary parameter calculated under a rainy regime of

TABLE 2. Summary of simulation parameters.

Parameter	Value
Carrier frequency	26 GHz, 38 GHz and 73 GHz
Site size (ℓ_s)	500 m
UE/AP heights (h_{UE}/h_{AP})	1.5 m/15 m
UEs velocity (v_{UE})	1.6 m/s
Angle between adjacent rays ($\Delta\theta$)	0.135°
Maximum number of reflections	7
Maximum number of APs (M)	50
Maximum number of users (K)	15
Link polarization	Vertical-Vertical
Downlink average power (P_d)	200 mW
Uplink power (P_p)	100 mW
Bandwidth (B)	20 MHz
Noise power spectral density	-174 dBm/Hz
AP/UE noise figure	6 dB
Amplifier efficiency ($a_m, \forall m$)	0.4
Antenna consumption ($P_{tc;m}, \forall m$)	0.2 W
Backhaul consumption ($P_{0;m}, \forall m$)	0.825 W
Traffic comsumption ($\rho_{bt;m}, \forall m$)	0.25 W/Gbits/s

C_r mm/hour. The $D_X(C_r)$ factor of the respective parameters for $C_r = 100$ mm/hour are presented in Table 4.

Analyzing the results presented in Table 3, it can be observed that the path loss is characterized by propagation exponents of approximately 1.8 and 4.1 for LoS and NLoS links, respectively. The propagation exponent grows as the rainy regimes become more intense. As shown in Table 4, the maximum growth observed in this parameter is equal to 0.22 in NLoS channels at 73 GHz. The shadow fading standard deviation also grows with the increase of the rainfall rate, with a maximum increment of 1.85 dB in NLoS channels at 73 GHz. The streets canyons geometry favors the origin of reflected components with high gain, resulting in relatively low Rice factors, with averages ranging between 1.83 dB (26 GHz) and 2.34 dB (73 GHz) in scenarios without rain. The Rice factor statistics remain approximately stable in the range between 0 mm/hour and 100 mm/hour, with a maximum increase on the average of only 0.13 dB for channels at 73 GHz, as seen in Table 4. The LoS probability is characterized with parameter d_1 varying between 16.1 m (26 GHz) and 19.1 m (73 GHz) and parameter d_2 defined between 26.4 m (26 GHz) and 18.3 m (73 GHz). Fig. 7 shows the LoS probability curves of the simulation data and the respective model for 73 GHz channels. The LoS probability results have good adherence with the model, with a root-mean-square error (RMSE) equal to 0.0183.

Analyzing the results for non-rainy scenarios in Table 3, the RMS-DS is higher in obstructed links, with an average value equal to 50.93 ns in NLoS channels at 38 GHz. This value decreases by 4.63 ns in a rainy regime of 100 mm/hour, as described in Table 4. In general, the RMS-DS statistics decrease with the increase of the rainfall rate, indicating a smaller temporal dispersion in heavy rain scenarios. Based on the RMS-DoS statistics shown in Table 3, it can be noticed that the propagation in street canyons promotes, on average, a greater spectral dispersion (Doppler domain) in

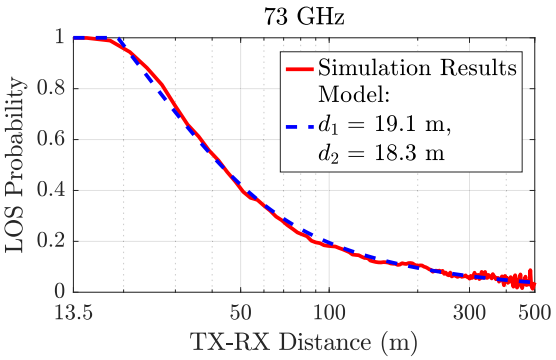

FIGURE 7. Simulation results and model of the LoS probability as a function of the TX-RX separation distance for channels in 73 GHz.

links with visibility due to the reception of strong reflected components. For example, RMS-DoS averages of 73 GHz channels are 73.93 Hz and 45.30 Hz on LoS and NLoS links, respectively. As can be seen in Table 4, as the rainfall rate increases, the RMS-DoS statistics slightly decrease, reaching a reduction on the average of 1.44 Hz for 73 GHz LoS channels. The calculated coherence lengths τ_c on the 26 GHz, 38 GHz and 73 GHz carriers are equal to 197, 136, and 75, respectively.

From the ray tracing simulations, the total rain attenuation values (Ω_r) are extracted from each link to statistically characterize rain attenuation. It is important to point out that, by fixing the frequency and the rain rate, the variables that influence Ω_r in this analysis are the length and direction of the paths and the polarization tilt angle. As an example, Fig. 8 shows the rain attenuation (expressed in linear units) histograms for $C_r = 10$ mm/hour and $C_r = 100$ mm/hour on 73 GHz channels. In this case, the average attenuations are 0.76 for light rain (10 mm/hour) and 0.27 for torrential rain (100 mm/hour). The histograms are superimposed by the respective lognormal distributions that best fit the results. For 10 mm/hour, the lognormal parameters are $\mu_\Omega = -0.3$ and $\sigma_\Omega = 0.1$. For 100 mm/hour, the parameters are $\mu_\Omega = -1.5$ and $\sigma_\Omega = 0.7$. In turn, Fig. 9 presents the sample average and standard deviation curves of Ω_r (expressed in dB) as a function of the rainfall rate. Analyzing the case with 1% exceedance probability, *i.e.*, $C_r = 63.6$ mm/hour, channels at 73 GHz suffer from an average rain attenuation equal to -4.1 dB with a standard deviation of 2.3 dB.

According to the results, the large-scale fading in dry scenarios, $\breve{\beta}_{m,k}$, is statistically correlated with Ω_r for $C_r > 0$ mm/hour. This numerical correlation occurs due to the dependence of both parameters on the path length. Fig. 10 presents the curves of the correlation coefficient between $\breve{\beta}_{m,k}$ and Ω_r, denoted as $r_{\beta,\Omega}$, as a function of the rainfall rate. These curves are calculated with $\breve{\beta}_{m,k}$ and Ω_r expressed in linear units. The values of $r_{\beta,\Omega}$ are positive, indicating an increasing dependence between the parameters. Furthermore, the correlation coefficient increases with the frequency and rainfall rate, reaching a maximum value equal to 0.6 in channels at 73 GHz.

TABLE 3. Channel parameters and statistics in a non-rainy regime ($C_r = 0$ mm/hour) obtained from ray tracing simulations.

Channel Parameter		Frequency					
		26 GHz		38 GHz		73 GHz	
		LoS	NLoS	LoS	NLoS	LoS	NLoS
Path Loss Exponent - κ		1.85	4.16	1.85	4.18	1.86	4.17
Shadow Fading STD - σ_χ (dB)		1.31	13.71	1.30	13.73	1.28	14.27
Rice Factor - $F_{m,k}$	Avg. (dB)	1.83	–	2.01	–	2.34	–
	STD. (dB)	4.77	–	5.06	–	5.49	–
LoS Probability	d_1 (m)	16.1		16.8		19.1	
	d_2 (m)	26.4		24.9		18.3	
RMS-DS - $\sigma_{\tau;m,k}$	Avg. (ns)	16.20	50.51	15.97	50.93	15.30	48.40
	STD. (ns)	14.53	67.22	14.50	68.29	13.97	64.25
RMS-DoS - $\sigma_{\nu;m,k}$	Avg. (Hz)	26.86	16.39	38.95	23.80	73.93	45.30
	STD. (Hz)	14.53	20.45	30.63	29.61	58.70	56.33
Coherence Length - τ_c		197		136		75	

TABLE 4. $D_X(C_r)$ factors of the respective channel parameters and statistics for $C_r = 100$ mm/hour.

$D_X(C_r)$ Factor							
Channel Parameter		Frequency					
		26 GHz		38 GHz		73 GHz	
		LoS	NLoS	LoS	NLoS	LoS	NLoS
Path Loss Exponent - κ		0.08	0.13	0.12	0.19	0.17	0.22
Shadow Fading STD - σ_χ (dB)		0.37	1.03	0.66	1.52	1.07	1.85
Rice Factor - $F_{m,k}$	Avg. (dB)	0.06	–	0.09	–	0.13	–
	STD. (dB)	0.04	–	0.06	–	0.09	–
RMS-DS - $\sigma_{\tau;m,k}$	Avg. (ns)	-1.82	-3.20	-2.43	-4.63	-2.90	-5.09
	STD. (ns)	-2.23	-6.47	-3.02	-9.30	-3.66	-8.72
RMS-DoS - $\sigma_{\nu;m,k}$	Avg. (Hz)	-0.28	-0.25	-0.58	-0.55	-1.44	-1.39
	STD. (Hz)	-0.14	-0.24	-0.30	-0.54	-0.74	-1.46

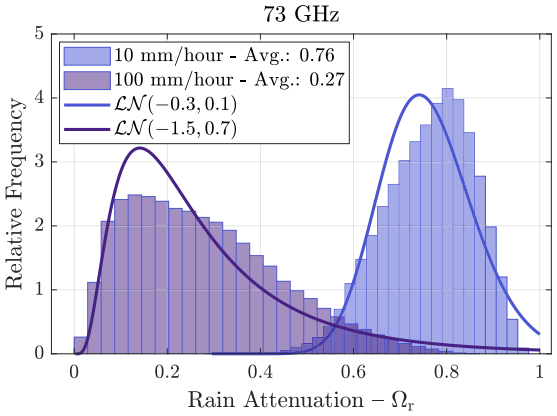

FIGURE 8. Rain attenuation histograms for 73 GHz channels considering $C_r = 10$ mm/hour and $C_r = 100$ mm/hour. The histograms are superimposed by the lognormal distributions that best fit the results.

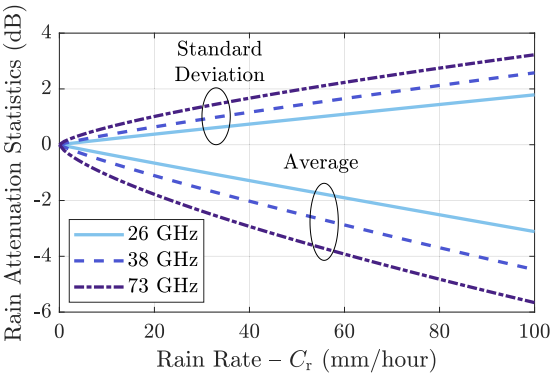

FIGURE 9. Rainfall attenuation statistics as a function of rainfall rate.

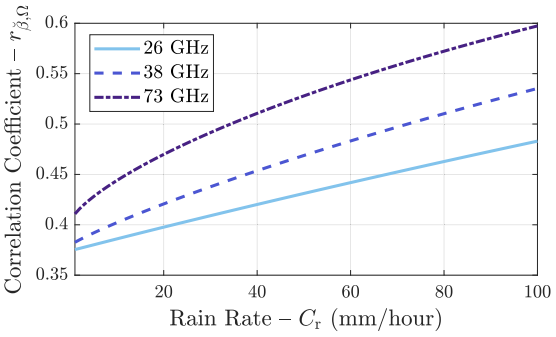

FIGURE 10. Correlation coefficient between $\check{\beta}_{m,k}$ and Ω_r.

B. PERFORMANCE RESULTS

In this subsection, the CF networks performance results are analyzed. Tables 5 and 6 show the SE, SSE and EE average values for different network configurations in non-rainy environments at a fixed $\tau_p = 5$. For a network serving $K = 5$ users, it is observed that doubling the number of antennas in the APs, on average, the SE increases by 0.85 bits/s/Hz, the SSE is incremented by 4.22 bits/s/Hz and the EE decreases 0.70 Mbits/J. For $K = 15$, case under the effect of pilot contamination, when doubling the value of L, the average values of the SE, SSE and EE are added by 0.78 bits/s/Hz, 11.57 bits/s/Hz and -1.65 Mbits/J, respectively. As shown in Table 3, propagation conditions tend to be more severe

TABLE 5. CF network performance parameters for $K = 5$ and $\tau_p = 5$ in non-rainy scenarios ($C_r = 0$ mm/hour).

CF Parameters			Avg. SE	Avg. SSE	Avg. EE
f (GHz)	M	L	(bits/s/Hz)	(bits/s/Hz)	(Mbits/J)
26	30	16	4.4	21.5	3.1
		32	5.2	25.6	2.2
		64	6.1	29.8	1.4
	50	16	5.2	25.8	2.2
		32	6.1	30.3	1.5
		64	7.0	35.0	1.0
38	30	16	4.2	20.9	3.0
		32	5.1	24.8	2.1
		64	5.9	28.9	1.4
	50	16	5.1	25.3	2.2
		32	5.9	29.7	1.5
		64	6.9	34.2	1.0
73	30	16	4.0	19.4	2.8
		32	4.7	23.2	2.0
		64	5.5	27.0	1.3
	50	16	4.8	24.0	2.1
		32	5.7	28.2	1.4
		64	6.5	32.6	0.9

TABLE 6. CF network performance parameters for $K = 15$ and $\tau_p = 5$ in non-rainy scenarios ($C_r = 0$ mm/hour).

CF Parameters			Avg. SE	Avg. SSE	Avg. EE
f (GHz)	M	L	(bits/s/Hz)	(bits/s/Hz)	(Mbits/J)
26	30	16	3.6	52.4	7.3
		32	4.3	63.4	5.3
		64	5.1	74.6	3.4
	50	16	4.4	66.2	5.5
		32	5.3	78.9	3.9
		64	6.1	91.5	2.5
38	30	16	3.5	51.2	7.1
		32	4.3	62.0	5.1
		64	5.0	72.9	3.3
	50	16	4.4	65.3	5.4
		32	5.2	77.7	3.8
		64	6.0	90.2	2.5
73	30	16	3.3	48.2	6.7
		32	4.0	58.4	4.8
		64	4.8	68.9	3.2
	50	16	4.2	62.0	5.1
		32	5.0	74.0	3.7
		64	5.8	86.2	2.4

as the carrier frequency increases. So, fixing the network configuration, the performance metrics at 73 GHz are the worst. For comparison purposes, it can be calculated that, in equivalent CF systems, the average difference between the SE, SSE and EE of networks operating at 26 GHz and 73 GHz are 0.36 bits/s/Hz, 3.57 bits/s/Hz and 0.23 Mbits/J, respectively. Fig. 11 and 12 respectively show the SSE and EE empirical cumulative distribution functions (ECDF) for different carriers, considering $M = 50$, $K = 15$, $\tau_p = 5$ and $L \in \{16, 32, 64\}$. The performance differences for networks operating at different frequencies are evident in these figures, in which it is observed that 26 GHz is the carrier that allows better SSE and EE conditions in the evaluated systems.

Denoting the average SSE and EE as a function of the rainfall rate by $\bar{S}_{CF}(C_r)$ and $\bar{E}_{CF}(C_r)$, respectively; the impact of rainfall attenuation on these parameters is measured by the

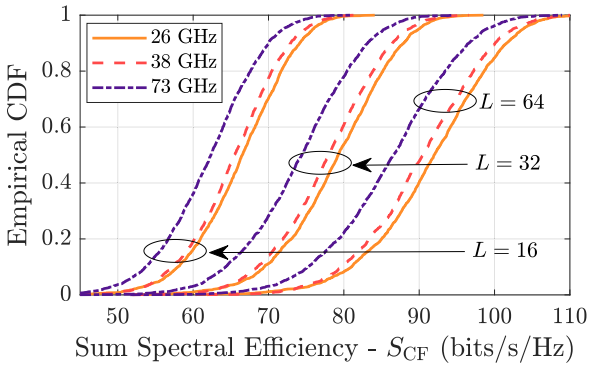

FIGURE 11. SSE ECDFs for $M = 50$, $K = 15$, $\tau_p = 5$ and $L \in \{16, 32, 64\}$.

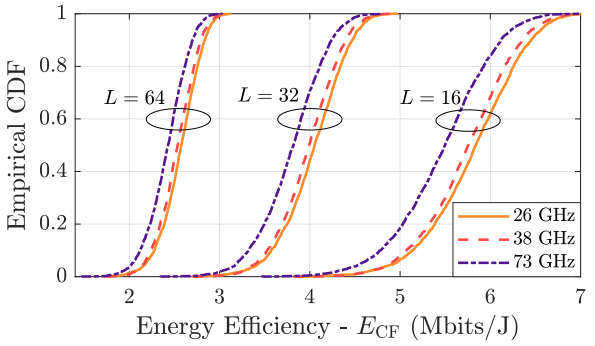

FIGURE 12. EE ECDFs for $M = 50$, $K = 15$, $\tau_p = 5$ and $L \in \{16, 32, 64\}$.

differences

$$\Delta_{SSE}(C_r) = \bar{S}_{CF}(C_r) - \bar{S}_{CF}(0) \tag{42}$$

and

$$\Delta_{EE}(C_r) = \bar{E}_{CF}(C_r) - \bar{E}_{CF}(0), \tag{43}$$

in which $\bar{S}_{CF}(0)$ and $\bar{E}_{CF}(0)$ are the average SSE and EE in non-rainy scenarios ($C_r = 0$ mm/hour). Fig. 13 presents the curves of $\Delta_{SSE}(C_r)$ considering $L = 16$, $K = 5$, $\tau_p = 15$ and $M \in \{20, 30, 40, 50\}$. It can be noted that the density of APs in the network influences the impact of rainfall attenuation on the average SSE. The probability of an user locating in the vicinity of a group of APs is greater in a denser network. This implies that denser networks suffer less impact from rain attenuation, since this is a phenomenon dependent on the length of the links. For example, in networks operating at 73 GHz with a rainfall rate of 63.6 mm/hour (0.01% exceedance rate), the average SSE decreases by 0.87 bit/s/Hz when $M = 20$ (80 APs/km^2), while networks with $M = 50$ (200 APs/km^2) have a reduction of 0.61 bits/s/Hz. Similar observations can be made for the EE, as seen in Fig. 14, where the curves of $\Delta_{EE}(C_r)$ are presented. A network under rainy regime of 63.6 mm/hour operating at 73 GHz with $M = 20$ APs has a reduction in the average EE of 178.3 kbits/J. In a denser network, with $M = 50$ APs, the reduction in the average EE is equal to 48 kbits/J.

As commented in subsection III-A, the occurrence of a specific rainfall rate corresponds to a given probability

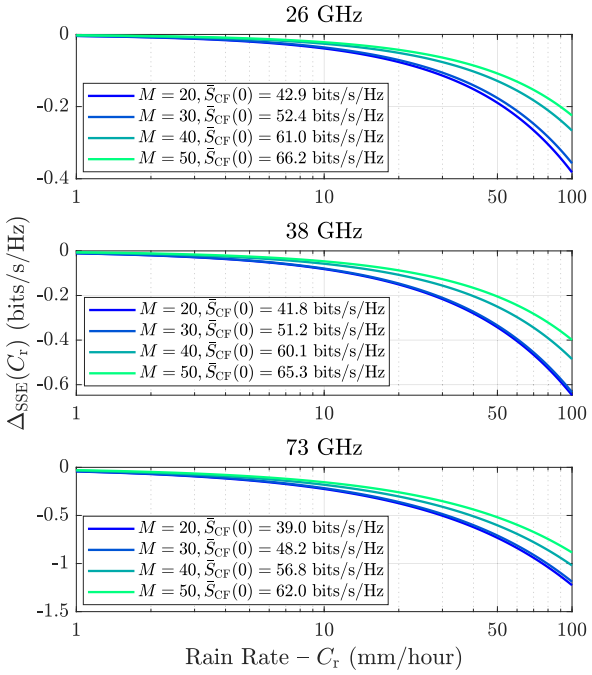

FIGURE 13. Average SSE variation curves as function of the rainfall rate ($\Delta_{\mathrm{SSE}}(C_{\mathrm{r}})$) considering $L = 16$, $K = 5$, $\tau_{\mathrm{p}} = 15$ and $M \in \{20, 30, 40, 50\}$.

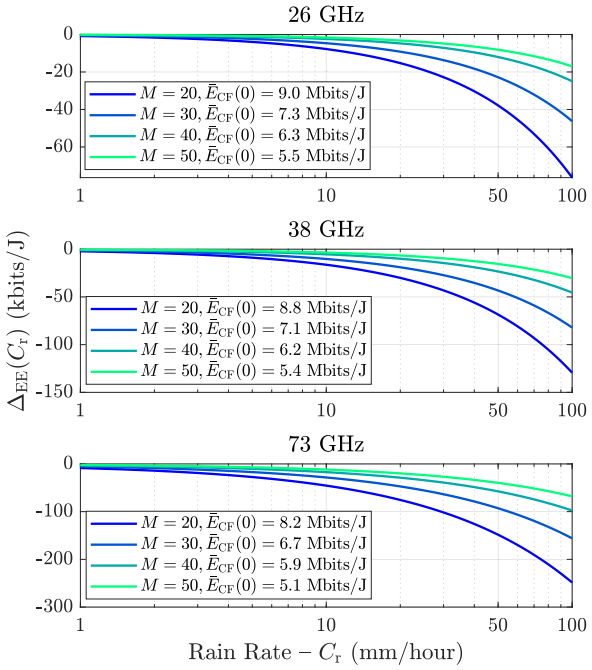

FIGURE 14. Average EE variation curves as function of the rainfall rate ($\Delta_{\mathrm{EE}}(C_{\mathrm{r}})$) considering $L = 16$, $K = 5$, $\tau_{\mathrm{p}} = 15$ and $M \in \{20, 30, 40, 50\}$.

of exceedance (see Fig. 3). Therefore, rain is a random event and its impact on a given percentage of annual time must be analyzed. For this, the exceedance probabilities of 0.1% and 0.01% are used as metrics, which correspond to precipitation rates of 21.5 mm/hour and 63.6 mm/hour, respectively. Table 7 presents the values of Δ_{SSE} and Δ_{EE} for the respective exceedance probabilities. These results

TABLE 7. Values of Δ_{SSE} and Δ_{EE} corresponding to the exceedance probabilities of 0.1% and 0.01% considering $K = 15$ and $\tau_{\mathrm{p}} = 5$.

CF Parameters			Δ_{SSE} (bits/s/Hz)		Δ_{EE} (kbits/J)	
f (GHz)	M	L	0.1%	0.01%	0.1%	0.01%
26	30	16	-0.08	-0.23	-9.86	-29.29
		32	-0.07	-0.22	-5.64	-17.12
		64	-0.06	-0.20	-2.66	-8.36
	50	16	-0.05	-0.14	-3.45	-10.55
		32	-0.03	-0.09	-1.19	-4.02
		64	-0.00	-0.02	-0.04	-0.35
38	30	16	-0.16	-0.42	-20.21	-54.29
		32	-0.16	-0.43	-12.21	-33.50
		64	-0.15	-0.41	-6.29	-17.78
	50	16	-0.09	-0.26	-7.05	-19.60
		32	-0.07	-0.20	-3.01	-9.06
		64	-0.03	-0.11	-0.62	-2.61
73	30	16	-0.38	-0.85	-49.74	-111.71
		32	-0.41	-0.93	-32.06	-72.94
		64	-0.42	-0.96	-18.30	-42.37
	50	16	-0.27	-0.63	-20.92	-48.01
		32	-0.25	-0.59	-11.44	-27.16
		64	-0.20	-0.50	-5.12	-12.93

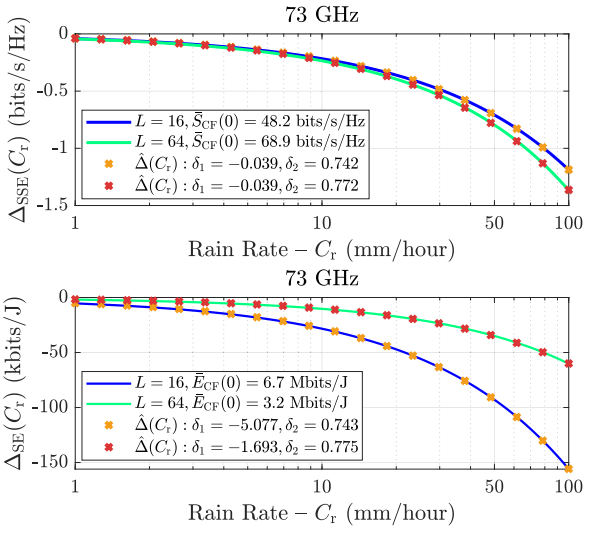

FIGURE 15. Curves of $\Delta_{\mathrm{SSE}}(C_{\mathrm{r}})$ and $\Delta_{\mathrm{EE}}(C_{\mathrm{r}})$ superimposed by the model expressed in (45) considering $L \in \{16, 64\}$, $K = 15$, $\tau_{\mathrm{p}} = 5$ and $M = 30$.

indicate the probability of exceedance of Δ_{SSE} and Δ_{EE} in an average year. For example, the probability of occurrence of a reduction greater than 0.5 bits/s/Hz in the average SSE caused by rain attenuation in networks operating at 73 GHz with $M = 50$ and $L = 64$ is 0.01%. On the same network, the probability of an average EE decrease of 12.93 kbits/J caused by rainy attenuation is 0.01%.

In addition to the absolute reduction in performance metrics, expressed by $\Delta_{\mathrm{SSE}}(C_{\mathrm{r}})$ and $\Delta_{\mathrm{EE}}(C_{\mathrm{r}})$, it may be useful to characterize the rate of change of these metrics with the rainfall intensity. For an arbitrary CF network, the computation of analytical expressions for $\Delta_{\mathrm{SSE}}(C_{\mathrm{r}})$ and $\Delta_{\mathrm{EE}}(C_{\mathrm{r}})$, as well as their derivatives, are difficult to demonstrate. However, it is observed that, for the cases studied in this work, the curves of $\Delta_{\mathrm{SSE}}(C_{\mathrm{r}})$ and $\Delta_{\mathrm{EE}}(C_{\mathrm{r}})$ can

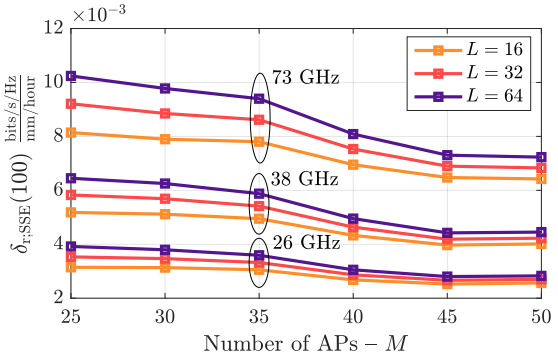

FIGURE 16. SSE average rate of decrease ($\delta_{r,SSE}(C_r)$) considering $C_r = 100$ mm/hour, $K = 5$, $\tau_p = 5$ and $L \in \{16, 32, 64\}$.

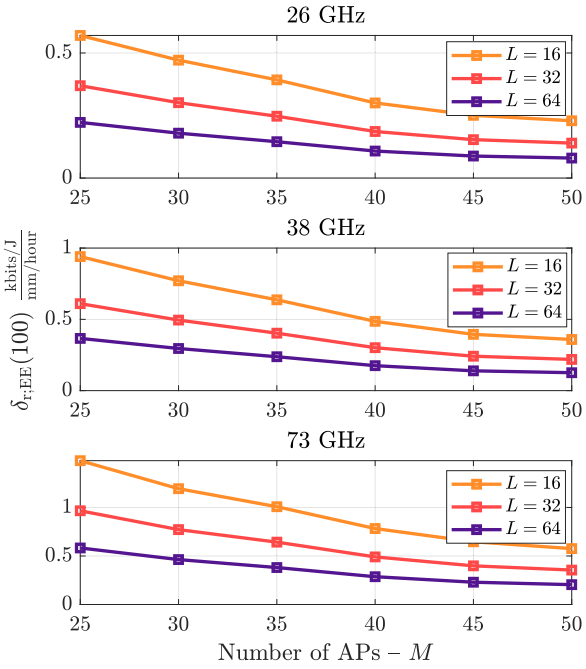

FIGURE 17. EE average rate of decrease ($\delta_{r,EE}(C_r)$) considering $C_r = 100$ mm/hour, $K = 5$, $\tau_p = 5$ and $L \in \{16, 32, 64\}$.

be approximated with good adherence by the expression

$$\hat{\Delta}(C_r) = \delta_1 \left(\frac{C_r}{1 \text{ mm/hour}} \right)^{\delta_2}, \tag{44}$$

in which $\delta_1 < 0$ and δ_2 are parameters found by a RMSE minimization procedure. In Fig. 15, curves of $\Delta_{SSE}(C_r)$ and $\Delta_{EE}(C_r)$ superimposed by the respective $\hat{\Delta}(C_r)$ models are shown. In these curves, the highest calculated RMSE is 0.135. Assuming that the expression in (44) represents the quantities $\Delta_{SSE}(C_r)$ and $\Delta_{EE}(C_r)$, the average rate of decrease of the SSE and EE in the interval of rainfall rate $[0, C_{r;f}]$ is calculated by

$$\delta_r(C_{r;f}) = -\frac{\hat{\Delta}(C_{r;f}) - \hat{\Delta}(0)}{C_{r;f}} = -\delta_1 C_{r;f}^{\delta_2 - 1}. \tag{45}$$

The minus sign (45) is used to indicate that SSE and EE decrease as C_r increases.

Fig. 16 and 17 show the SSE and EE average rate of change curves, respectively denoted as $\delta_{r,SSE}(C_r)$ and $\delta_{r,EE}(C_r)$, varying with the number of APs in the network considering $C_r = 100$ mm/hour, $K = 5$, $\tau_p = 5$ and $L \in \{16, 32, 64\}$. It can be noted that the increase in the number of APs (network densification) tends to make the CF network more resistant to the effect of rain attenuation. For example, a network operating at 73 GHz and with 25 APs, each one with $L = 64$ antennas, has an average rate of change of 10^{-2} $\frac{\text{bits/s/Hz}}{\text{mm/hour}}$, which indicates an average reduction of 1 bits/s/Hz in the SSE for $C_r = 100$ mm/hour. When $M = 50$, the rate reduces to 6×10^{-3} $\frac{\text{bits/s/Hz}}{\text{mm/hour}}$, indicating an average reduction of 0.6 bits/s/Hz in SSE. The same observation can be made for the EE results, in which the average change rate for $M = 25$ is 0.5 $\frac{\text{kbits/J}}{\text{mm/hour}}$ and for $M = 50$ it is 0.2 $\frac{\text{kbits/J}}{\text{mm/hour}}$.

V. CONCLUSION

This work presented a study of cell-free (CF) massive multiple-input multiple-output (mMIMO) networks operating in the millimeter wave (mmWave) spectrum under the effect of rain attenuation based on site-specific ray tracing simulations. The simulations were performed at 26 GHz, 38 GHz and 73 GHz, considering rainfall regimes with a maximum rate of 100 mm/hour. From the simulation results, the communications channel was characterized and network performance metrics were extracted. According to the simulation results, when doubling the number of antennas at each access point (AP), for the case of pilot contamination, the sum spectral efficiency (SSE) grows, on average, by 11.57 bits/s/Hz while the energy efficiency (EE) decreases by 1.65 Mbits/J, indicating a cost-benefit ratio regarding data rate and power consumption. As a consequence of the strict propagation conditions, with path loss exponent for non-light-of-sight (NLoS) links equal to 4.17, the operation at 73 GHz presents the worst performance indicators.

It was found that denser networks become more protected against rain attenuation regarding average SSE and EE. Due to the high probability of a given user being located in the vicinity of the APs, the effect of the distance dependent rain attenuation on the link becomes negligible in dense networks. However, the reduction in the average SSE and EE is small even on relatively sparse networks. For example, in networks with 20 APs (80 APs/km^2) operating at 73 GHz and serving five users, under the effect of a rain of 63.6 mm/hour, there is a reduction in the average SSE of only 0.87 bits/s/Hz. In addition to the reduced impact of rain attenuation on the overall system performance, the occurrence of rainy events capable of significantly degrading the system performance is highly unlikely. Considering the local meteorological data of the simulated propagation environment, the probability of occurrence of a rainy event capable of reducing the average SSE by more than 0.5 bit/s/Hz is only 0.01%, for a network operating at 73 GHz with 50 APs, each one equipped with 64 antennas. However, the probability of exceedance for a given rainfall rate varies geographically, and environments

with predisposition to violent rainfalls (>100 mm/hour) must be individually analyzed. The reduced impact of rain attenuation on CF networks is also confirmed by the SSE and EE low rates of decrease with the rainfall intensity. Rates of decrease in the order of 10^{-2} $\frac{\text{bits/s/Hz}}{\text{mm/hour}}$ and 0.5 $\frac{\text{kbits/J}}{\text{mm/hour}}$ were calculated for the mean SSE and EE, respectively; which indicates a low sensitivity of these metrics with the rain rate.

According to the results, the effects of rain attenuation on the performance of CF mmWave networks are negligible. However, it is worth noting that rainy events can still affect these networks by means of other mechanisms, such as the wet antenna effect and depolarization [75], [76]. Additionally, other weather conditions, like snow and fog, may also impact the performance of these networks when operating in the mmWave spectrum. To gain a more comprehensive understanding of the performance of mmWave CF networks under different weather conditions, it is essential to conduct further analysis. This investigation presents an opportunity for future work in this area. By exploring the impact of various weather conditions on the performance of mmWave CF networks it is possible to develop a more complete understanding of the factors that affect these networks. This knowledge can then be leveraged to develop more robust and reliable communication systems that can operate effectively in a wide range of weather conditions.

REFERENCES

[1] X. Wang, L. Kong, F. Kong, F. Qiu, M. Xia, S. Arnon, and G. Chen, "Millimeter wave communication: A comprehensive survey," *IEEE Commun. Surveys Tuts.*, vol. 20, no. 3, pp. 1616–1653, 3rd Quart., 2018.

[2] S. A. Busari, K. M. S. Huq, S. Mumtaz, L. Dai, and J. Rodriguez, "Millimeter-wave massive MIMO communication for future wireless systems: A survey," *IEEE Commun. Surveys Tuts.*, vol. 20, no. 2, pp. 836–869, 2nd Quart., 2018.

[3] M. Alsabah, M. A. Naser, B. M. Mahmmod, S. H. Abdulhussain, M. R. Eissa, A. Al-Baidhani, N. K. Noordin, S. M. Sait, K. A. Al-Utaibi, and F. Hashim, "6G wireless communications networks: A comprehensive survey," *IEEE Access*, vol. 9, pp. 148191–148243, 2021.

[4] M. A. Albreem, A. H. A. Habbash, A. M. Abu-Hudrouss, and S. S. Ikki, "Overview of precoding techniques for massive MIMO," *IEEE Access*, vol. 9, pp. 60764–60801, 2021.

[5] H. Q. Ngo, A. Ashikhmin, H. Yang, E. G. Larsson, and T. L. Marzetta, "Cell-free massive MIMO versus small cells," *IEEE Trans. Wireless Commun.*, vol. 16, no. 3, pp. 1834–1850, Jan. 2017.

[6] E. Nayebi, A. Ashikhmin, T. L. Marzetta, H. Yang, and B. D. Rao, "Precoding and power optimization in cell-free massive MIMO systems," *IEEE Trans. Wireless Commun.*, vol. 16, no. 7, pp. 4445–4459, Jul. 2017.

[7] E. Björnson and L. Sanguinetti, "Making cell-free massive MIMO competitive with MMSE processing and centralized implementation," *IEEE Trans. Wireless Commun.*, vol. 19, no. 1, pp. 77–90, Jan. 2020.

[8] S. Elhoushy and W. Hamouda, "Towards high data rates in dynamic environments using hybrid cell-free massive MIMO/small-cell system," *IEEE Wireless Commun. Lett.*, vol. 10, no. 2, pp. 201–205, Feb. 2021.

[9] H. Q. Ngo, L.-N. Tran, T. Q. Duong, M. Matthaiou, and E. G. Larsson, "Energy efficiency optimization for cell-free massive MIMO," in *Proc. IEEE 18th Int. Workshop Signal Process. Adv. Wireless Commun. (SPAWC)*, Jul. 2017, pp. 1–5.

[10] S. Elhoushy, M. Ibrahim, and W. Hamouda, "Cell-free massive MIMO: A survey," *IEEE Commun. Surveys Tuts.*, vol. 24, no. 1, pp. 492–523, 1st Quart., 2022.

[11] H. Q. Ngo, A. Ashikhmin, H. Yang, E. G. Larsson, and T. L. Marzetta, "Cell-free massive MIMO: Uniformly great service for everyone," in *Proc. IEEE 16th Int. Workshop Signal Process. Adv. Wireless Commun. (SPAWC)*, Jul. 2015, pp. 201–205.

[12] G. Femenias and F. Riera-Palou, "Cell-free millimeter-wave massive MIMO systems with limited fronthaul capacity," *IEEE Access*, vol. 7, pp. 44596–44612, 2019.

[13] G. Femenias and F. Riera-Palou, "Reduced-complexity downlink cell-free mmWave massive MIMO systems with fronthaul constraints," in *Proc. Eur. Signal Process. Conf.*, Sep. 2019, pp. 1–5.

[14] I.-S. Kim, M. Bennis, and J. Choi, "Cell-free mmWave massive MIMO systems with low-capacity fronthaul links and low-resolution ADC/DACs," *IEEE Trans. Veh. Technol.*, vol. 71, no. 10, pp. 10512–10526, Oct. 2022.

[15] M. Ibrahim, S. Elhoushy, and W. Hamouda, "Uplink performance of mmWave-fronthaul cell-free massive MIMO systems," *IEEE Trans. Veh. Technol.*, vol. 71, no. 2, pp. 1536–1548, Feb. 2022.

[16] P. H. T. da Silva, R. M. Duarte, H. S. Silva, M. S. Alencar, and W. J. L. De Queiroz, "Evaluation of cell-free millimeter-wave massive MIMO systems based on site-specific ray tracing simulations," *IEEE Access*, vol. 10, pp. 82092–82105, 2022.

[17] T. S. Rappaport, S. Sun, R. Mayzus, H. Zhao, Y. Azar, K. Wang, G. N. Wong, J. K. Schulz, M. Samimi, and F. Gutierrez, "Millimeter wave mobile communications for 5G cellular: It will work!" *IEEE Access*, vol. 1, pp. 335–349, 2013.

[18] A. N. Uwaechia and N. M. Mahyuddin, "A comprehensive survey on millimeter wave communications for fifth-generation wireless networks: Feasibility and challenges," *IEEE Access*, vol. 8, pp. 62367–62414, 2020.

[19] M. Xiao, S. Mumtaz, Y. Huang, L. Dai, Y. Li, M. Matthaiou, G. K. Karagiannidis, E. Björnson, K. Yang, and A. Ghosh, "Millimeter wave communications for future mobile networks," *IEEE J. Sel. Areas Commun.*, vol. 35, no. 9, pp. 1909–1935, Sep. 2017.

[20] A. Ghosh, T. A. Thomas, M. C. Cudak, R. Ratasuk, P. Moorut, F. W. Vook, T. S. Rappaport, G. R. MacCartney, S. Sun, and S. Nie, "Millimeter-wave enhanced local area systems: A high-data-rate approach for future wireless networks," *IEEE J. Sel. Areas Commun.*, vol. 32, no. 6, pp. 1152–1163, Jun. 2014.

[21] Agência Nacional de Telecomunicações (Anatel). (Mar. 2019). *Anatel Aprova Agenda Regulatória 2019–2020*. Accessed: May 30, 2022. [Online]. Available: https://www.gov.br/anatel/pt-br/assuntos/noticias/anatel-aprova-agendaregulatoria-2019-2020

[22] M. A. Samad, F. D. Diba, and D.-Y. Choi, "A survey of rain attenuation prediction models for terrestrial links-current research challenges and state-of-the-art," *Sensors*, vol. 21, no. 4, pp. 1–28, Feb. 2021.

[23] E. Alozie, A. Abdulkarim, I. Abdullahi, A. D. Usman, N. Faruk, I.-F. Y. Olayinka, K. S. Adewole, A. A. Oloyede, H. Chiroma, O. A. Sowande, L. A. Olawoyin, S. Garba, A. L. Imoize, A. Musa, Y. A. Adediran, and L. S. Taura, "A review on rain signal attenuation modeling, analysis and validation techniques: Advances, challenges and future direction," *Sustainability*, vol. 14, no. 18, pp. 1–65, Sep. 2022.

[24] R. S. Tenório, M. C. da Silva Moraes, and H. Sauvageot, "Raindrop size distribution and radar parameters in coastal tropical rain systems of northeastern Brazil," *J. Appl. Meteorol. Climatol.*, vol. 51, no. 11, pp. 1960–1970, Nov. 2012.

[25] F. Norouzian, E. Marchetti, M. Gashinova, E. Hoare, C. Constantinou, P. Gardner, and M. Cherniakov, "Rain attenuation at millimeter wave and low-THz frequencies," *IEEE Trans. Antennas Propag.*, vol. 68, no. 1, pp. 421–431, Jan. 2020.

[26] *Recommendation ITU-R P.838-3: Specific Attenuation Model for Rain for Use in Prediction Methods*, document P.530-18, ITU-R, Mar. 2005.

[27] H. T. P. da Silva, R. M. Duarte, M. S. de Alencar, and W. J. L. Queiroz, "Cell-free at millimeter wave frequency simulation using the ray tracing method," in *Proc. 14th Eur. Conf. Antennas Propag. (EuCAP)*, Mar. 2020, pp. 1–5.

[28] M. R. Akdeniz, Y. Liu, M. K. Samimi, S. Sun, S. Rangan, T. S. Rappaport, and E. Erkip, "Millimeter wave channel modeling and cellular capacity evaluation," *IEEE J. Sel. Areas Commun.*, vol. 32, no. 6, pp. 1164–1179, Apr. 2014.

[29] M. K. Samimi and T. S. Rappaport, "Ultra-wideband statistical channel model for non line of sight millimeter-wave urban channels," in *Proc. IEEE Global Commun. Conf. (GLOBECOM)*, Dec. 2014, pp. 3483–3489.

[30] T. Imai, "A survey of efficient ray-tracing techniques for mobile radio propagation analysis," *IEICE Trans. Commun.*, vol. E100.B, no. 5, pp. 666–679, 2017.

[31] S. Kasdorf, B. Troksa, C. Key, J. Harmon, and B. M. Notaros, "Advancing accuracy of shooting and bouncing rays method for ray-tracing propagation modeling based on novel approaches to ray cone angle calculation," *IEEE Trans. Antennas Propag.*, vol. 69, no. 8, pp. 4808–4815, Aug. 2021.

[32] S.-N. Jin, D.-W. Yue, and H. H. Nguyen, "Spectral and energy efficiency in cell-free massive MIMO systems over correlated Rician fading," *IEEE Syst. J.*, vol. 15, no. 2, pp. 2822–2833, Jun. 2021.
[33] Y. Zhang, M. Zhou, H. Cao, L. Yang, and H. Zhu, "On the performance of cell-free massive MIMO with mixed-ADC under Rician fading channels," *IEEE Commun. Lett.*, vol. 24, no. 1, pp. 43–47, Jan. 2020.
[34] *Recommendation ITU-R P.1623-1: Prediction Method of Fade Dynamics on Earth-Space Paths*, document P.1623-1, ITU-R, 2005.
[35] W. Fan, J. Zhang, E. Bjornson, S. Chen, and Z. Zhong, "Performance analysis of cell-free massive MIMO over spatially correlated fading channels," in *Proc. IEEE Int. Conf. Commun.*, May 2019, pp. 1–6.
[36] O. Ozdogan, E. Bjornson, and E. G. Larsson, "Massive MIMO with spatially correlated Rician fading channels," *IEEE Trans. Commun.*, vol. 67, no. 5, pp. 3234–3250, May 2019.
[37] O. Ozdogan, E. Bjoornson, and J. Zhang, "Cell-free massive MIMO with Rician fading: Estimation schemes and spectral efficiency," in *Proc. 52nd Asilomar Conf. Signals, Syst., Comput.*, Oct. 2018, pp. 975–979.
[38] X. Hu, C. Zhong, X. Chen, W. Xu, H. Lin, and Z. Zhang, "Cell-free massive MIMO systems with low resolution ADCs," *IEEE Trans. Commun.*, vol. 67, no. 10, pp. 6844–6857, Oct. 2019.
[39] H. Q. Ngo, L.-N. Tran, T. Q. Duong, M. Matthaiou, and E. G. Larsson, "On the total energy efficiency of cell-free massive MIMO," *IEEE Trans. Green Commun. Netw.*, vol. 2, no. 1, pp. 25–39, Mar. 2018.
[40] Z. Yun and M. F. Iskander, "Ray tracing for radio propagation modeling: Principles and applications," *IEEE Access*, vol. 3, pp. 1089–1100, 2015.
[41] S. Y. Seidel and T. S. Rappaport, "Site-specific propagation prediction for wireless in-building personal communication system design," *IEEE Trans. Veh. Technol.*, vol. 43, no. 4, pp. 879–891, Nov. 1994.
[42] J. G. Cleary and G. Wyvill, "Analysis of an algorithm for fast ray tracing using uniform space subdivision," *Vis. Comput.*, vol. 4, no. 2, pp. 65–83, Mar. 1988.
[43] H. T. P. da Silva, H. S. Silva, M. S. Alencar, W. J. L. Queiroz, and U. S. Dias, "Characterization of large-scale parameters in indoor THz channels applying the ray tracing method," in *Proc. Workshop Commun. Netw. Power Syst. (WCNPS)*, Nov. 2022, pp. 1–6.
[44] C. A. Balanis, *Antenna Theory—Analysis and Design*, 3rd ed. Hoboken, NJ, USA: Wiley, 2005.
[45] *Recommendation ITU-R P.676-13: Attenuation by Atmospheric Gases and Related Effects*, document P.676-13, ITU-R, Aug. 2022.
[46] I. Rodriguez, R. Abreu, E. P. L. Almeida, M. Lauridsen, A. Loureiro, and P. Mogensen, "24 GHz cmWave radio propagation through vegetation: Suburban tree clutter attenuation," in *Proc. 10th Eur. Conf. Antennas Propag. (EuCAP)*, Apr. 2016, pp. 1–5.
[47] *Recommendation ITU-R P.833-10: Attenuation in Vegetation*, document P.833-10, ITU-R, Sep. 2021.
[48] F. Sheikh, Y. Gao, and T. Kaiser, "A study of diffuse scattering in massive MIMO channels at terahertz frequencies," *IEEE Trans. Antennas Propag.*, vol. 68, no. 2, pp. 997–1008, Feb. 2020.
[49] R. J. Luebbers, "A heuristic UTD slope diffraction coefficient for rough lossy wedges," *IEEE Trans. Antennas Propag.*, vol. 37, no. 2, pp. 206–211, Feb. 1989.
[50] M. Schneider and R. J. Luebbers, "A general, uniform double wedge diffraction coefficient," *IEEE Trans. Antennas Propag.*, vol. 39, no. 1, pp. 8–14, Jan. 1991.
[51] P. Pathak, "High frequency techniques for antenna analysis," *Proc. IEEE*, vol. 80, no. 1, pp. 44–65, Jan. 1992.
[52] L. da Silva Mello and M. S. Pontes, "Unified method for the prediction of rain attenuation in satellite and terrestrial links," *J. Microw., Optoelectron. Electromagn. Appl.*, vol. 11, no. 1, pp. 1–14, 2012.
[53] H. Singh, V. Kumar, K. Saxena, B. Boncho, and R. Prasad, "Proposed model for radio wave attenuation due to rain (RWAR)," *Wireless Pers. Commun.*, vol. 115, no. 1, pp. 791–807, Jun. 2020.
[54] C. Capsoni, F. Fedi, and A. Paraboni, "A comprehensive meteorologically oriented methodology for the prediction of wave propagation parameters in telecommunication applications beyond 10 GHz," *Radio Sci.*, vol. 22, no. 3, pp. 387–393, May 1987.
[55] *Recommendation ITU-R P.837-7: Characteristics of Precipitation for Propagation Modelling*, document P.676-13, ITU-R, Jun. 2017.
[56] L. Luini, G. Roveda, M. Zaffaroni, M. Costa, and C. G. Riva, "The impact of rain on short *E*-band radio links for 5G mobile systems: Experimental results and prediction models," *IEEE Trans. Antennas Propag.*, vol. 68, no. 4, pp. 3124–3134, Apr. 2020.
[57] L. Luini and C. Capsoni, "MultiEXCELL: A new rain field model for propagation applications," *IEEE Trans. Antennas Propag.*, vol. 59, no. 11, pp. 4286–4300, Nov. 2011.
[58] A. A. H. Budalal, M. R. Islam, K. Abdullah, and T. A. Rahman, "Modification of distance factor in rain attenuation prediction for short-range millimeter-wave links," *IEEE Antennas Wireless Propag. Lett.*, vol. 19, no. 6, pp. 1027–1031, Jun. 2020.
[59] A. A. Yusuf, A. Falade, B. J. Olufeagba, O. O. Mohammed, and T. A. Rahman, "Statistical evaluation of measured rain attenuation in tropical climate and comparison with prediction models," *J. Microw., Optoelectron. Electromagn. Appl.*, vol. 15, no. 2, pp. 123–134, Jun. 2016.
[60] J. Huang, Y. Cao, X. Raimundo, A. Cheema, and S. Salous, "Rain statistics investigation and rain attenuation modeling for millimeter wave short-range fixed links," *IEEE Access*, vol. 7, pp. 156110–156120, 2019.
[61] Z. A. Shamsan, "Rainfall and diffraction modeling for millimeter-wave wireless fixed systems," *IEEE Access*, vol. 8, pp. 212961–212978, 2020.
[62] OpenStreetMap Contributors. (2022). *Planet Dump*. [Online]. Available: https://www.openstreetmap.org
[63] *Recommendation ITU-R P.2040-2: Effects of Building Materials and Structures on Radiowave Propagation Above About 100 MHz*, document P.2040-2, ITU-R, Jun. 2021.
[64] J. E. Jaselskis, J. Grigas, and A. Brilingas, "Dielectric properties of asphalt pavement," *J. Mater. Civil Eng.*, vol. 15, no. 5, pp. 427–434, Oct. 2003.
[65] I. Kusák and M. Lunak, "Impedance spectroscopy—New tool for testing ceramic roofing tiles buildings materials," in *Proc. NDE*, Nov. 2009, pp. 1–10.
[66] B. Langen, G. Lober, and W. Herzig, "Reflection and transmission behaviour of building materials at 60 GHz," in *Proc. 5th IEEE Int. Symp. Pers., Indoor Mobile Radio Commun., Wireless Netw.-Catching Mobile Future*, vol. 2, Sep. 1994, pp. 505–509.
[67] J. Zhang, S. Chen, Y. Lin, J. Zheng, B. Ai, and L. Hanzo, "Cell-free massive MIMO: A new next-generation paradigm," *IEEE Access*, vol. 7, pp. 99878–99888, 2019.
[68] H. Yang and T. L. Marzetta, "Energy efficiency of massive MIMO: Cell-free vs. cellular," in *Proc. IEEE 87th Veh. Technol. Conf.*, Jun. 2018, pp. 1–5.
[69] Z. Zhou, X. Gao, J. Fang, and Z. Chen, "Spherical wave channel and analysis for large linear array in LoS conditions," in *Proc. IEEE Globecom Workshops*, Dec. 2015, pp. 1–6.
[70] *Study on Channel Model for Frequencies From 0.5 to 100 GHz*, 3GPP, document 38.901, Mar. 2022.
[71] G. L. Stüber, *Principles of Mobile Communication*, 4th ed. Atlanta, GA, USA: Springer, 2017.
[72] A.-A.-A. Boulogeorgos, J. M. Riera, and A. Alexiou, "On the joint effect of rain and beam misalignment in terahertz wireless systems," *IEEE Access*, vol. 10, pp. 58997–59012, 2022.
[73] S. Sun, T. A. Thomas, T. S. Rappaport, H. Nguyen, I. Z. Kovacs, and I. Rodriguez, "Path loss, shadow fading, and line-of-sight probability models for 5G urban macro-cellular scenarios," in *Proc. IEEE Globecom Workshops (GC Wkshps)*, Dec. 2015, pp. 1–7.
[74] B. Sklar, "Rayleigh fading channels in mobile digital communication systems," *IEEE Commun. Mag.*, vol. 35, no. 7, pp. 90–100, Jul. 1997.
[75] K. Pu, X. Liu, and H. He, "Wet antenna attenuation model of *E*-band microwave links based on the LSTM algorithm," *IEEE Antennas Wireless Propag. Lett.*, vol. 19, no. 9, pp. 1586–1590, Sep. 2020.
[76] A. Paraboni, A. Martellucci, C. Capsoni, and C. G. Riva, "The physical basis of atmospheric depolarization in slant paths in the V band: Theory, Italsat experiment and models," *IEEE Trans. Antennas Propag.*, vol. 59, no. 11, pp. 4301–4314, Nov. 2011.

HIGO THAIAN P. DA SILVA was born in Nova Floresta, Paraíba, Brazil, in 1993. He received the B.Sc. degree in electrical engineering from the Federal University of Paraíba, in 2016, and the M.Sc. degree in electrical engineering from the Federal University of Campina Grande, Brazil, in 2018, where he is currently pursuing the D.Sc. degree. His research interests include signal processing and the channel modeling of wireless communication.

HUGERLES S. SILVA (Member, IEEE) received the B.Sc., M.Sc., and Ph.D. degrees in electrical engineering from the University Federal of Campina Grande, Brazil, in 2014, 2016, and 2019, respectively. He is currently an Adjunct Professor with the University of Brasília. His main research interests include wireless communications, digital signal processing, and wireless channel modeling.

MARCELO S. ALENCAR (Senior Member, IEEE) received the bachelor's degree in electrical engineering from Universidade Federal de Pernambuco (UFPE), Brazil, in 1980, the master's degree in electrical engineering from Universidade Federal da Paraiba (UFPB), Brazil, in 1988, and the Ph.D. degree from the University of Waterloo, Canada, in 1994. He was with the Department of Electrical Engineering, UFPB, the Federal University of Campina Grande (UFCG), the State University of Santa Catarina (UDESC), and the Federal University of Bahia (UFBA). He was a Visiting Professor with the University of Toronto. He is currently a Visiting Professor with Senai Cimatec, Salvador, Brazil. He is also the Founder and President of the Institute for Advanced Studies in Communications (Iecom). He was a Columnist for the traditional Brazilian newspaper *Jornal do Commercio*. He published more than 500 engineering and scientific papers and 26 books. He also wrote chapters for 12 books. He served on the Board of Directors for SBrT and the SBMO Council. He has been awarded several scholarships and grants from the Brazilian National Council for Scientific and Technological Research (CNPq), the IEEE Foundation, the University of Waterloo, and the Federal University of Paraiba. He received the Achievement Award from the Brazilian Telecommunications Society (SBrT), the Award from the Medicine College, UFCG, and the Achievement Award from the College of Engineering, UFPE. He is a Laureate of the prestigious 2014 Attilio Giarola Medal from the Brazilian Microwave and Optoelectronics Society (SBMO). He is a registered Professional Engineer.

WAMBERTO J. L. DE QUEIROZ received the M.Sc. degree in electrical engineering from the Federal University of Paraiba, Campina Grande, Brazil, in 2000, and the D.Sc. degree in electrical engineering from the Federal University of Campina Grande, Campina Grande, in 2004. He was an Adjunct Professor with the Federal University of Ceará, from 2007 to 2010, and has been an Associate Professor with the Federal University of Campina Grande, since May 2020. His current research interests include digital communications over fading channels, channel modeling and simulations, spectrum sensing systems, and estimation theory.

UGO SILVA DIAS (Senior Member, IEEE) was born in Belém, Pará, Brazil, in 1981. He received the B.Sc. degree in electrical engineering from the Federal University of Pará, Brazil, in 2004, and the M.Sc. and Ph.D. degrees in electrical engineering from the State University of Campinas, Brazil, in 2006 and 2010, respectively. Since March 2010, he has been a Professor with the University of Brasilia (UnB), Brazil. He is currently a Faculty Member with the Department of Electrical Engineering. He has been involved on the organizing committee of several conferences. He is a Senior Member of the Brazilian Telecommunications Society (SBrT) and a member of the IEEE Communications Society and the Brazilian Communications Committee. He is a Productivity Research Fellow of the National Council of Scientific and Technological Development (CNPq), Brazil. He serves as the Vice-President for the SBrT, the Chair for the IEEE ComSoc CN Brazil Chapter, and an Advisor for the IEEE ComSoc UnB Student Branch Chapter. He acts as a Scientific Consultant for CNPq.